

Real-Time Image Analysis Software

Suitable for Resource-Constrained Computing

Alexandre Matov^{1, †}

¹ DataSet Analysis LLC, 155 Jackson St, San Francisco, CA 94111, United States

[†] Corresponding author:
email: matov@datasetanalysis.com

Key words: Real-Time Detection and Feature Tracking, On The Fly Image Analysis, Medical Software, Diagnostic Software, Resource-Constrained Computing, Multiplatform Software, Smartphones Software, Smart Glasses Software

ABSTRACT

Introduction: Methods for personalizing medical treatment are the focal point of contemporary clinical research. In cancer care, for instance, we can analyze the effects of therapies at the level of individual cells. Complete characterization of treatment efficacy and evaluation of why some individuals respond to specific regimens, whereas others do not, requires additional approaches to genetic sequencing at single time points. Methods for the continuous analysis of changes in phenotype, such as morphology and motion tracking of cellular proteins and organelles over time frames spanning the minute-hour scales, can provide important insight to patient treatment options. The integration of measurements of intracellular dynamics and the contribution of multiple genetic pathways in degenerative diseases is vital for the development of biomarkers for the early detection of pathogenesis and therapy efficacy.

Methods: We have developed a software suite (DataSet Tracker) for real-time analysis designed to run on computers, smartphones, and smart glasses hardware and suitable for resource-constrained, on-the-fly computing in microscopes without internet connectivity; a demo is available for viewing at datasetanalysis.com. Our objective is to present the community with an integrated, easy to use by all, tool for resolving the complex dynamics of the cytoskeletal meshworks, intracytoplasmic membranous networks, and vesicle trafficking. Our software is optimized for resource-constrained computing and can be installed even on microscopes without internet connectivity.

Results: Our computational platform can provide high-content analyses and functional secondary screening of novel compounds that are in the process of approval, or at a pre-clinical stage of development, and putative combination therapies based on FDA-approved drugs. Importantly, dissecting the mechanisms of drug action with quantitative detail will allow the design of drugs that impede relapse and optimal dose regimens with minimal harmful side effects by carefully exploiting disease-specific aberrations.

Conclusions: DataSet Tracker, the real-time optical flow feature tracking software presented in this contribution, can serve as the base module of an integrated platform of existing and future algorithms for real-time cellular analysis. The computational assay we propose could successfully be applied to evaluate treatment strategies for any human organ. It is our goal to have this integrated tool approved for use in the clinical practice.

INTRODUCTION

We present software for real-time image analysis. The algorithms were tested on personal computers, cell phones, and smart glasses. The objective of this work is to facilitate research work, primarily in live cell biology, during which scientists are required to utilize multi-step customized processes in order to analyze imaging data. All existing software packages analyze images off-line, meaning that researchers collect imaging datasets, for example using high resolution microscopy, and then transfer the data, often comprising large size files, to another computer where they need access to specialized software tools for different analyses.

Our interest is to streamline this process in two ways. (1) By offering real-time analysis tools, which, because there will no longer be a need to transfer data, it would save an enormous amount of time. Our objective is to integrate different computer vision modules in one single package with multiple analysis modules that perform a variety of functions. Such integration will eliminate the need to load imaging data in different software tools one by one sequentially, as it is often done in science labs at present. (2) Because our software displays analysis results in real time (5 frames per second for the examples shown in the manuscript), that would allow us to improve the calibration of experimental conditions, such as drug treatment regimens. The reason for this is that the changes in the behavior of biological cells can be measured, with quantitative detail, during sample manipulation and image acquisition. These measurements will allow for the first time to identify subtle changes in biological function, which cannot

be observed by the naked eye. This way, the real-time software will enhance our understanding of human physiology and the regulation of individual cells.

The complex dynamics of cytoskeletal proteins make them a difficult subject of study without quantitative analytical tools. The *ex vivo* analysis of living patient-derived cells comprises of the evaluation of the response of cytoskeletal filaments and meshworks, intracytoplasmic membranous networks, and vesicle trafficking before and after drug treatment and requires motion tracking. Tracking is the process of finding object (feature) motion correspondence from one time-lapse frame to the next throughout a time-lapse sequence. The features can be fluorescently labeled proteins or imaged label-free using a microscopy technique that highlights the gray-scale intensity gradient to their immediate surroundings in the image. Methods that can reliably analyze the evolution of the morphology and localization of cellular proteins over hundreds of time-lapse frames will be very relevant for capturing the changes in the subcellular organization in disease and during treatment (Matov, 2024e; Matov, 2025a; Matov, 2025b; Matov et al., 2010; Matov and Bacconi, 2024; Matov et al., 2011). Such methods allow physicians to compare visually and quantitatively the effects of treatment regimens and select the one most likely to be efficacious.

Alternatively, intercellular dynamic behavior can be analyzed with available computer vision robotics libraries, which deliver results in real-time. On-the-fly image analysis and instant quantitative feedback can significantly speed up clinical work and allow for the precise calibration of the imaging set-up and optimization of the drug regimens based on considerations of their effects on cell function. To improve on the ability to precisely calibrate the set-up, augmented reality artificial intelligence software can be added to existing live-cell microscopes, thus providing instant feedback during sample observation and image acquisition. The selection of drug dose and deducing its effects, depending on the dose administered, is a daunting task. During treatment of tubulin inhibitors, for instance, different

microtubule (MT)-associated proteins are activated depending on the drug dose administered, and consequently, different resistance mechanisms may be triggered. The effects of MT inhibitors change nonlinearly with a dose increase. While a high dose of nocodazole depolymerizes MTs, a low dose, which could lead to no side effects, increases polymerization rates (Thoma et al., 2010). Also, while a high dose of paclitaxel stabilizes MTs, a low dose similarly increases MT polymerization rates (Matov, 2024e). Real-time analysis software will allow to store tracking results during sample observation and this way, it will allow the detailed documentation and quantification of all observations made by a scientist.

Our work has been focused on the automated analysis of cytoskeletal dynamics, predominantly those of MTs (Gatlin et al., 2010; Gatlin et al., 2009; Houghtaling et al., 2009) and filamentous actin (F-actin) (Adams et al., 2004; Ponti et al., 2005), to study the effects of tubulin, actin, and tropomyosin inhibitors and post-translational modifications as well as modulation of focal adhesions (FAs) (Spanjaard et al., 2015) and ectopic activation of GSK3 β (Kumar et al., 2009). During pathogenesis, or as a result of drug treatment in disease, cells change their intracellular organization, rearrange their internal components as they grow, divide, and adapt mechanically to a hostile environment. These functions depend on protein filaments (the cytoskeleton and FAs), which provide the cell shape and its capacity for directed movement.

The main novelty presented in the manuscript is related to the ability to quantify and visualize, in real time, the changes in morphology and motion of cellular components as the cell adapts to a wide range of biochemical and mechanical perturbations. We have investigated these changes in the context of the two main cytoskeletal proteins, tubulin and actin. Tubulin has been the target of numerous therapeutic approaches for six decades now. Most of these therapies have been, in essence, a “black box” approach,

where a treatment with debilitating side effects is administered, without having the ability to anticipate whether it would affect the desired target.

With our approach, an instant quantitative evaluation of some of the more difficult to visually interpret effects of tubulin-targeting compounds can be performed while calibrating the imaging set-up and during image acquisition, which will facilitate deducing mechanistic explanations for the reasons behind the measured differences. Actin, for instance, is instrumented in wound healing as well as during tumor metastasis; it is also the most important protein in heart and other muscle function. Very few drugs currently modulate actin activity directly, albeit the abundant availability of anti-inflammatory medications which affect the COX pathway. It is the variability of patient response in genomics precision medicine that underscores the importance of utilizing quantitative imaging techniques in the clinic.

There is a lot we do not know about the regulation of our organs, the cells comprising them, and the interdependencies between them. The validation of novel prognostic and predictive biomarkers can be done by comparing the *ex vivo* tumor growth kinetics and treatment predictions to outcomes of patients with similar, to primary cells after treatment, genetic profiles, which are enrolled in clinical trials.

RESULTS

Segmentation of cellular areas

Taxane treatment induces a variety of changes in cancer cells, including changes in MT polymer density. Differences in baseline polymer density exist also between drug-sensitive and drug-resistant cells. To quantify such differences, we quantify the overall MT intensity in images of A549 lung cancer cells before and after knockdown of BRCA1 (B1KD). Because such cells grow in clusters, we use nuclear labeling to segment the areas of the individual cells (see Materials and Methods). The B1KD

cells are systematically dimmer and appear to have a lower level of MT density in comparison to the drug-resistance parental A549 cells (Fig. 1). This result suggests that reduced MT polymer density correlates with improved sensitivity to taxane treatment in lung cancer.

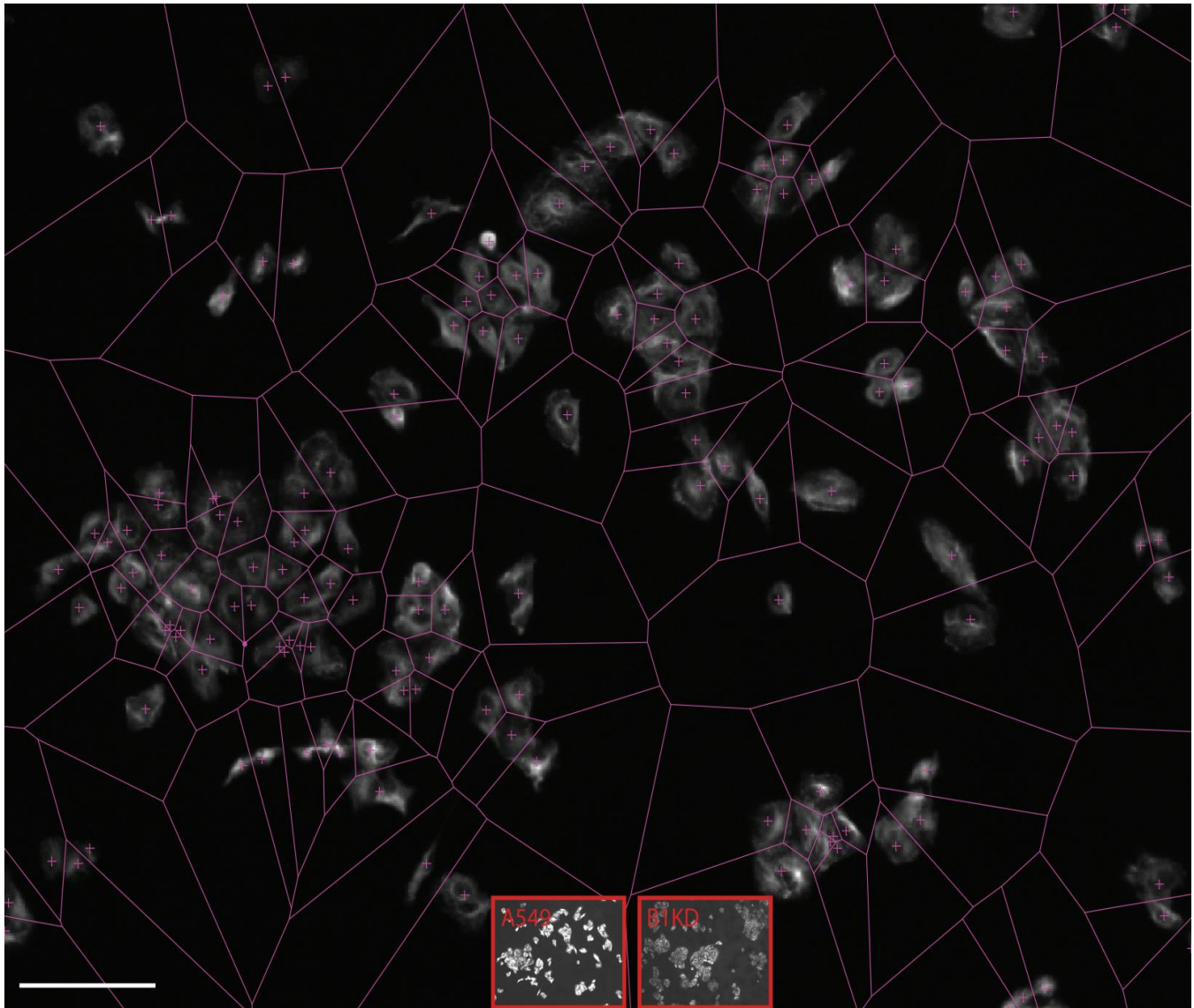


Figure 1. Segmentation of the area of A549 lung cancer cells. Tubulin is fluorescently labeled. The figure presents an image segmentation approach to determine the boundaries between cells growing in clusters. Scale bar equals 40 μm . The insets show a comparison between the intensity in parental A549 cells and a BRCA1 knockdown cells, which appear dimmer.

To further investigate resistance to treatment with tubulin inhibitors, we performed a sulforhodamine B colorimetric assay for cytotoxicity screening (Vichai and Kirtikara, 2006) in MDA-MB-231 and SK-BR-3 breast cancer cell lines. Low doses of paclitaxel (about 2 nM) and docetaxel (0.2 nM), contraintuitively, increased with up to 18% (paclitaxel) or 24% (docetaxel) the cell density in these cell lines, indicating increased cell proliferation to result from drug treatment at low concentrations. In addition, the portion of the cytoplasmic area of breast cancer cells was considerably larger compared to the nucleus than in prostate cancer cell lines and patient-derived CTCs, based on PSMA and DAPI staining (Fig. 2). This is an indication that the extent of the MT networks varies between different types of epithelial tumors, which indicates susceptibility of different types of tubulin inhibitors, such as polymer destabilizes in lung and breast cancer, and polymer stabilizers in prostate cancer.

Microtubules modulate the composition of tumor secretome

Cancer cells activate their surrounding fibroblasts to promote remodeling of their microenvironment (Potenta et al., 2008). Taxane treatment attenuates fibroblast motility in HMF3S cells and reduces the levels of lysyl oxidase homologue 2, c-Met, fibronectin, TGF β , CTGF, importin α , and 14-3-3 in MDA-MB-231 cells (Tran et al., 2013; Tran et al., 2012). TGF β is a key driver of tumor progression and extracellular matrix remodeling and we used lipopolysaccharide (LPS) stimulation to stimulate secretion of TGF β (Xie et al., 2009) and analyzed cell membrane-associated TGF β in populations of both untreated or treated with paclitaxel non-permeabilized cells (see Materials and Methods). In untreated MDA-MB-231 cells, LPS stimulation resulted in an increase of bright foci of TGF β at the cell membrane, reflecting accumulation of TGF β -containing secretory granules on the cell surface. In contrast, paclitaxel treated MDA-MB-231 cells did not exhibit increased TGF β plasma membrane localization upon LPS stimulation. Overall, paclitaxel-mediated stabilization of MTs in breast cancer cells inhibited the trafficking and secretion of TGF β (Fig. 3). These data indicate that tubulin inhibitors directly affect trafficking of TGF β -containing granules to the cell membrane.

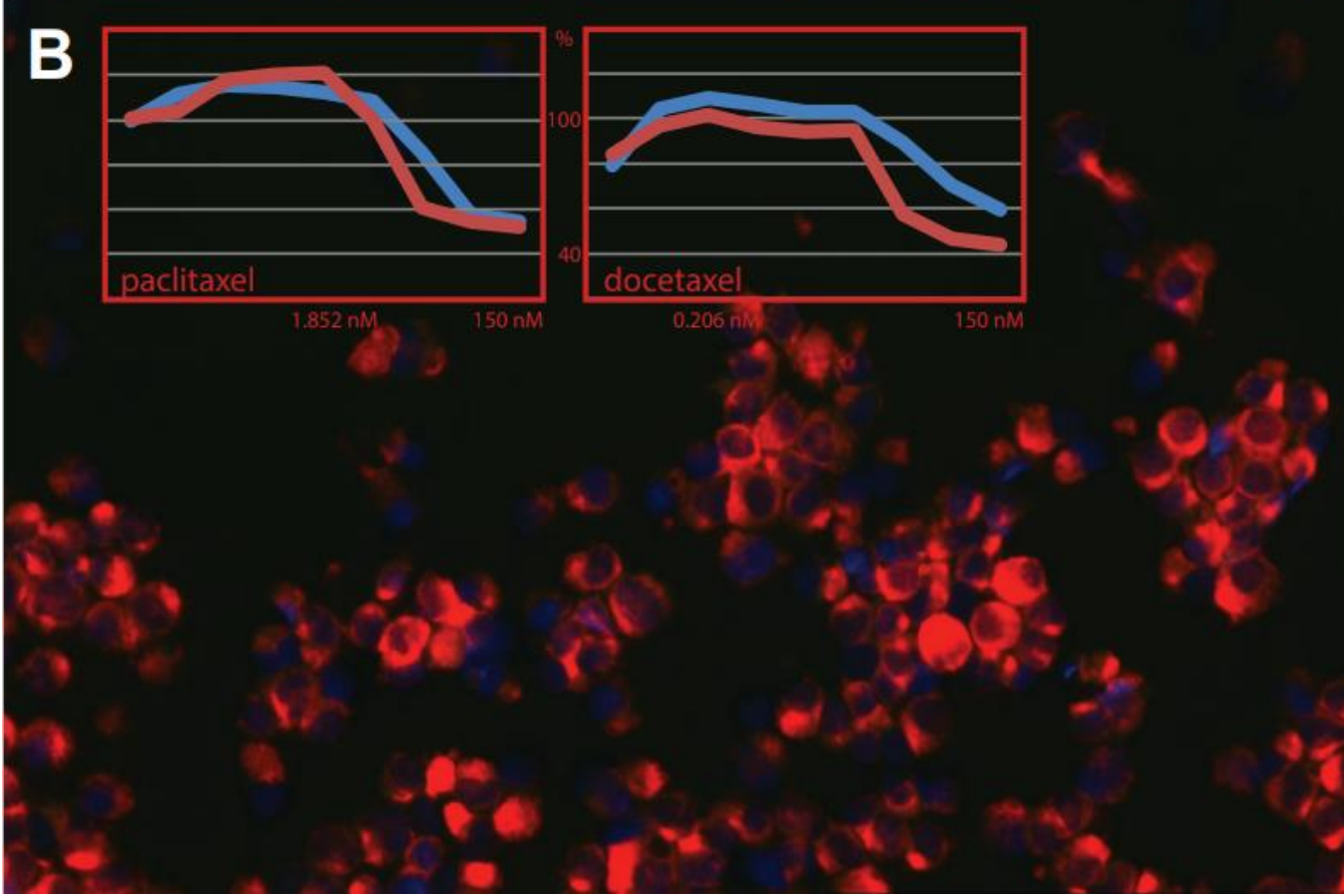
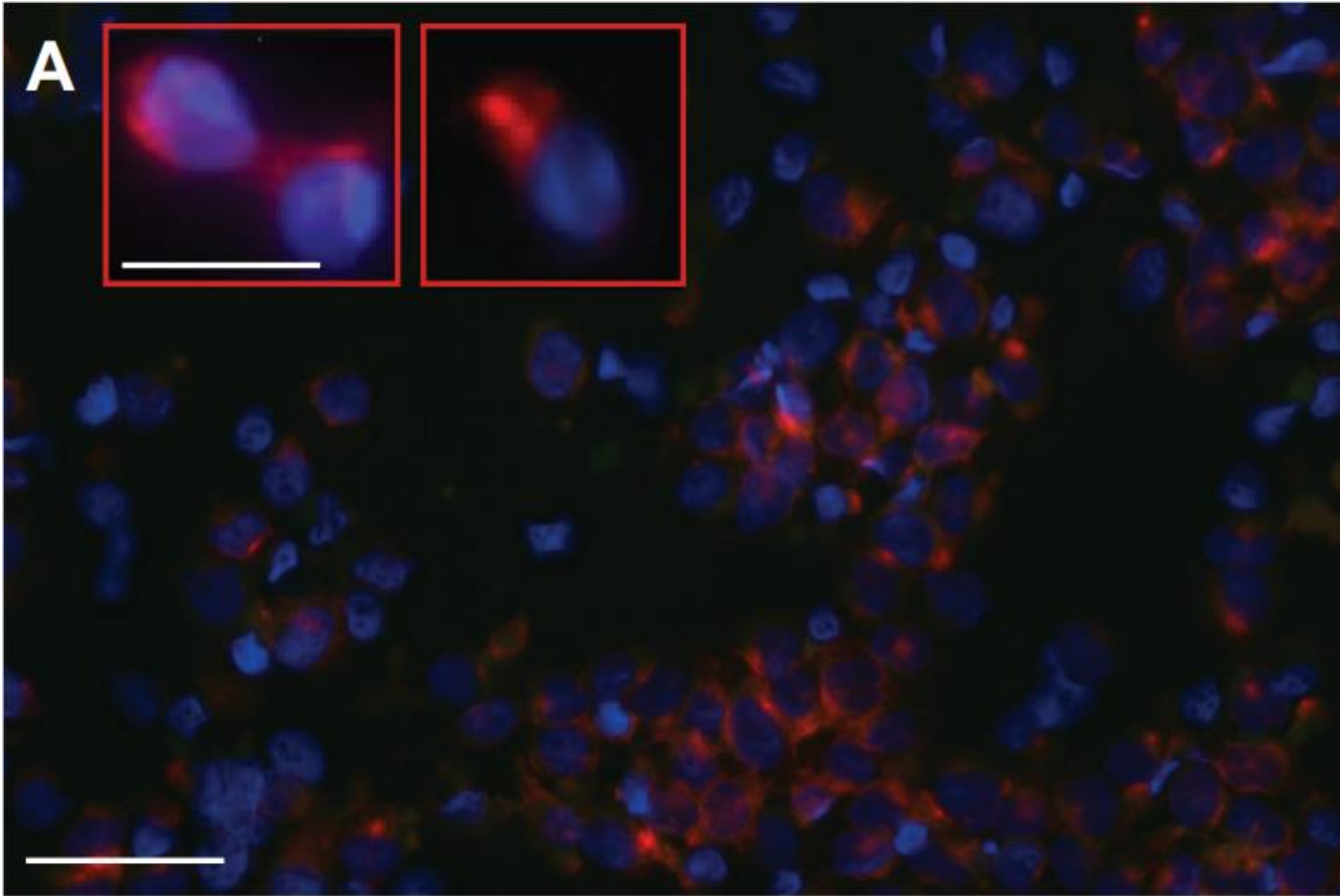


Figure 2. Cell density and extent of the cytoplasm in cancer cells. Figure legend: PSMA (J591, tumor marker, red), CD45 (leukocyte marker, green), DAPI (nuclear marker, blue). Scale bar equals 70 μm . (A) LNCaP prostate cancer cells. Inset: Androgen-independent prostate cancer CTCs. Inset scale bar equals 20 μm . (B) MDA-MB-231 breast cancer cells. The insets show cell density determination values based on a sulforhodamine B cytotoxicity assay for MDA-MB-231 (blue line) and SK-BR-3 breast cancer (red line) cells after titration with two tubulin inhibitors.

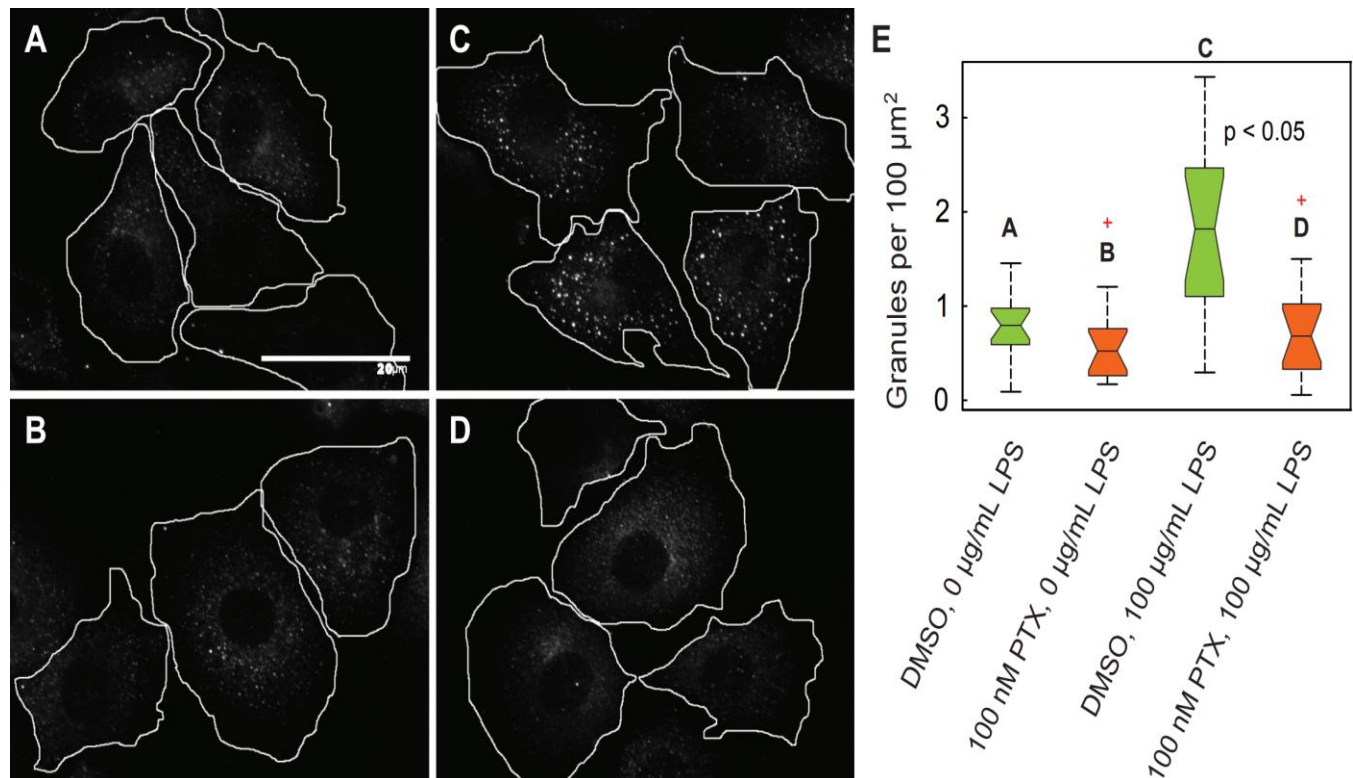


Figure 3. Paclitaxel treatment prevented trafficking of intracellular TGF β to the cell surface in MDA-MB-231 cells. (A-D) Detection of TGF β at the cell membrane by immunofluorescence in non-permeabilized MDA-MB-231 cells stimulated with 100 $\mu\text{g/mL}$ lipopolysaccharide (LPS) stimulation followed by vehicle (DMSO) or 100 nM paclitaxel (PTX) treatment. See also the x-axis labels in (E). White solid lines denote the segmented cell boundaries. Three to five cells were analyzed per condition. Scale bar equals 20 μm . (E) Distributions of the number of TGF β -stained foci on the cell surface.

Sensitivity of diffuse gastric cancer cells to docetaxel

Although taxane-based therapy is approved for advanced gastric cancer, a majority of patients exhibit intrinsic resistance to taxanes and require additional lines of therapy (Shitara et al., 2020). Identifying methods to predict resistance would spare the individuals predisposed not to respond to taxanes from the side effects. Intestinal and diffuse gastric cancer are the two major intrinsic genomic subtypes with distinct patterns of gene expression. Intestinal cell lines are significantly more sensitive to 5-fluorouracil

and oxaliplatin, but more resistant to cisplatin, than the diffuse cell lines (Tan et al., 2011). In this context, to investigate the sensitivity to taxanes in diffuse gastric cancer, we performed titration experiments with eight diffuse gastric cancer cell lines and compared their sensitivity to docetaxel. In all three sensitive cell lines (TMK1, SNU1, and AZ521), the cell survival was less than 50% for docetaxel concentrations of 10 nM and higher, and the MT network formed bundles (Fig. 4). These data suggest the use of a docetaxel and cisplatin regimen for gastric cancers with mutated *TP53*.

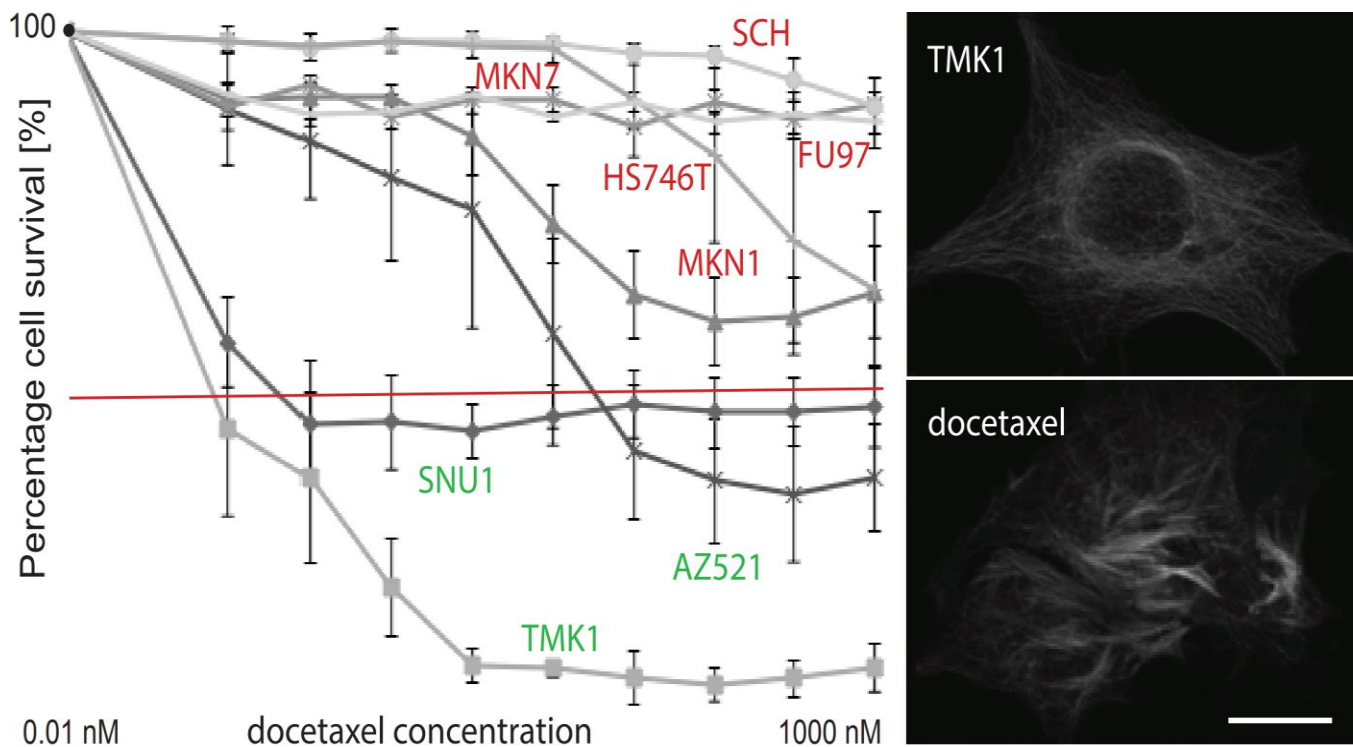


Figure 4. Sensitivity to docetaxel in diffuse gastric cancer cell lines. The figure shows cell survival curves for eight cell lines treated with increasing doses of docetaxel. The right panels show the MT cytoskeleton in a drug-sensitive TMK1 cell before (upper panel) and after (lower panel) treatment with 100 nM docetaxel. Scale bar equals 10 μ m. Magnification, 63x.

Cell proliferation dynamics follow a Gompertz function (Gompertz, 1825; Winsor, 1932). Further, the growth of patient-derived organoids seeded from single cells could undergo a bifurcation point in gene expression (Bratsun et al., 2005; Gillespie, 2007) and either continue exponentially or undergo cell death (Matov, 2024g). After drug treatment, there is a lag in the consequential reduction in organoid size,

resembling a hysteresis cycle (Ewing, 1881), which can be utilized as a metric for drug efficacy evaluation. To model tumor growth dynamics, we will model organoid growth as a Markov chain with absorbing states and will use Bayes rules statistics (Bremaud, 1999; Matov, 1999).

Enumeration of circulating tumor cells

The molecular mechanisms underlying taxane resistance in prostate cancer have not been well elucidated due to the limitations in available tumor tissue to study. Circulating tumor cells (CTCs) represent a liquid biopsy of the tumors and CTC isolation can lead to molecular characterizations potentially revealing predictive biomarkers for taxane sensitivity or resistance. A ficolling technology is used to isolate live CTCs from whole blood of prostate cancer patients. These cells are plated onto an 8 mm coverslip and subsequently stained for three labels used for enumeration at low magnification: DAPI to label the cell nucleus, prostate specific membrane antigen (PSMA) is used as positive CTC identifier, CD45 labels the leukocytes and is therefore used as negative CTC identifier. Using these three labels, we aim at differentiating the prostate cells from white blood cells isolated from the blood's buffy coat.

To this end, we developed a computer vision algorithm for the automated analysis of blood samples (see Materials and Methods). In brief, it is based on wavelet segmentation to perform detection of local intensity clusters through a combination of multiscale products (Starck et al., 2000) and denoising by iterative filtering of significant coefficients (Olivo-Marin, 2002). Our analysis enumerates the number of CTCs in patient blood and an example for one of the 50 positions (with three detected CTCs) resulting from imaging a coverslip at 10x magnification is shown on Fig. 5. We will aim at correlating this information with taxane efficacy in patients to develop a predictive algorithm that can identify taxane resistant patients before they receive treatment. Altogether, this computational approach connects exciting basic science with clinically relevant concepts and customized chemotherapy.

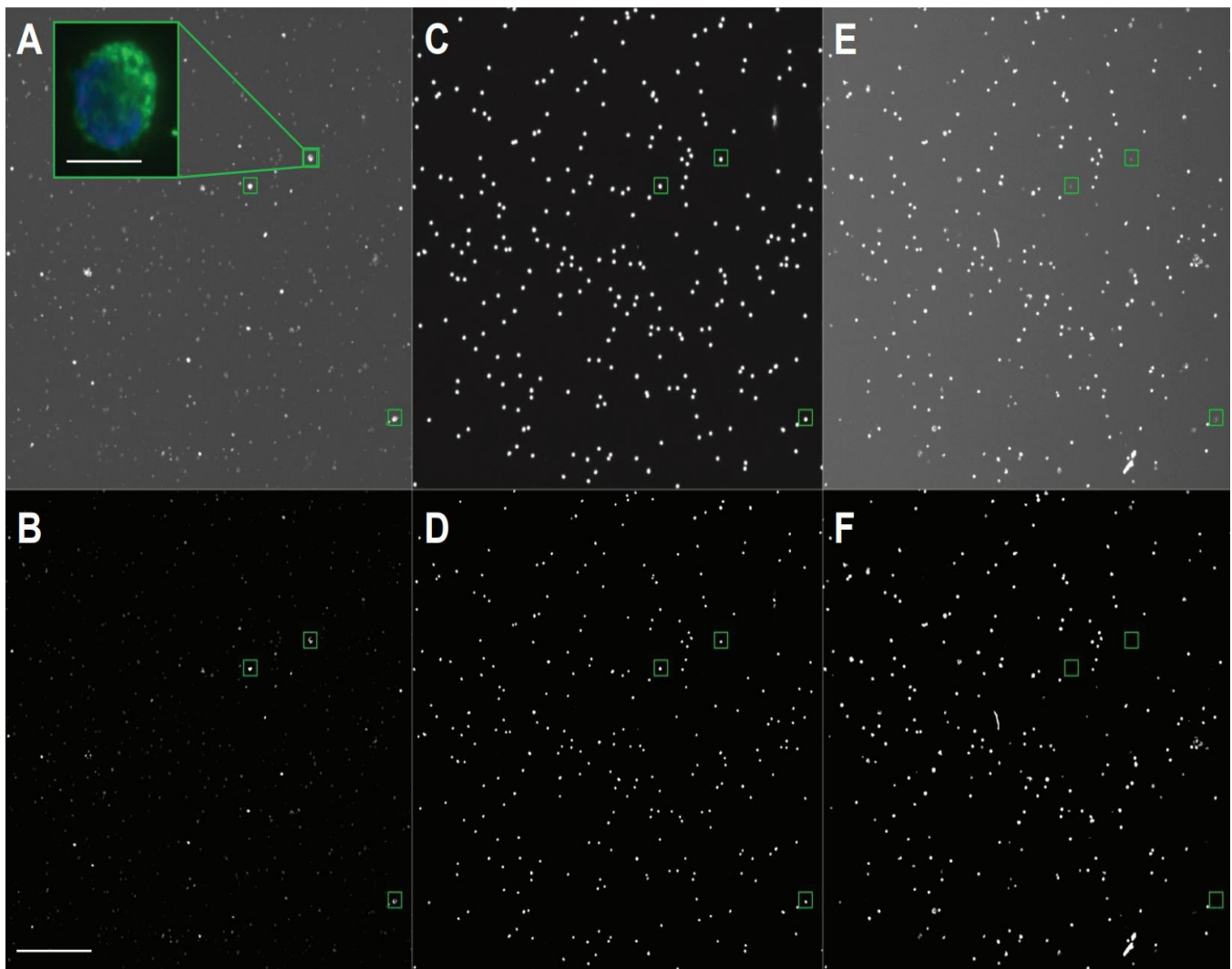


Figure 5. Enumeration of patient CTCs in samples imaged on coverslips. The figure (showing 1 of 50 images for the coverslip) demonstrates an approach for the detection of CTCs of metastatic prostate cancer patients imaged with multi-color microscopy. (A) PSMA labeling. (B) Segmentation of the PSMA image shown in (A). (C) DAPI labeling of nuclear areas. (D) Segmentation of nuclei shown in (C). (E) CD45 labeling of leukocytes. (F) Segmentation of the CD45 image shown in (E) The tumor cells are detected as PSMA+/DAP+/CD45- cells and marked with green squares. Scale bar equals 200 μm . Magnification, 10x. Inset figure legend: PSMA (muJ591, tumor marker, green), DAPI (nuclear marker, blue). Scale bar equals 20 μm . Magnification, 40x.

Patient-derived organoids

Patient-derived organoids are small organ-mimetics that better recapitulate, compared to cell lines, *in vivo* responses to treatments. Organoids can be derived from patient CTCs and tissue biopsies, and we worked with prostate and colorectal tumor samples. In our experience, lentiviral transduction allows for fluorescent markers to be introduced and imaged in patient cells forming organoids within 14 hours after

surgery (Matov, 2024e; Matov, 2025a). Such clinically-relevant cultures can be utilized to support decisions regarding the choice of regimens in the context of anticipation of drug resistance. In prostate cancer, tubulin inhibitors are widely used in advanced disease without having precise predictions regarding their clinical efficacy in terms of both intrinsic and acquired resistance. Drug susceptibility can be evaluated *ex vivo* not only by direct analysis of patient tumor cells but also based on the response of adjacent to the tumor tissues. In primary prostate cancer (Fig. 6), this approach can be implemented by culturing adjacent benign epithelial cells as well as cancer-associated fibroblasts. In the metastatic setting, such evaluation can be accomplished also by analysis of cells in the host tissue. Cells from tissues of different origin, for example colorectal and lung, do not mix in organoids. We established organoids from both metastatic colorectal cancer cells and benign lung cells derived from a chest wall resection (Fig. 6). The availability of the cells from the tumor microenvironment, such as the extracellular matrix, can improve the precision of the analysis *ex vivo*.

Because of the limited amount of tumor tissue collected during biopsies, it is not feasible to perform the traditional toxicity assays, such as IC50 measurements. It is our hypothesis that assays related to killing tumor cells *ex vivo* do not faithfully represent the ability of the drug to cause patient tumors to recede. Furthermore, many primary prostate tumors are dormant and do not allow expansion *ex vivo*, and even in the case of proliferative cultures, with every passage the cells additionally diverge from the original tumor regulation. For these reasons, we propose the utilization of assays that demonstrate the engagement by the drugs of their cellular target without killing the organoids. Changes in protein morphology and dynamics in patient-derived cultures after drug treatment will, thus, become – upon clinical validation - metrics for drug susceptibility. This approach will improve our ability to anticipate drug resistance and spare patients that are not predisposed to respond to a certain drug the toxicity. In addition, it will allow us to identify an optimal drug regimen for each patient.

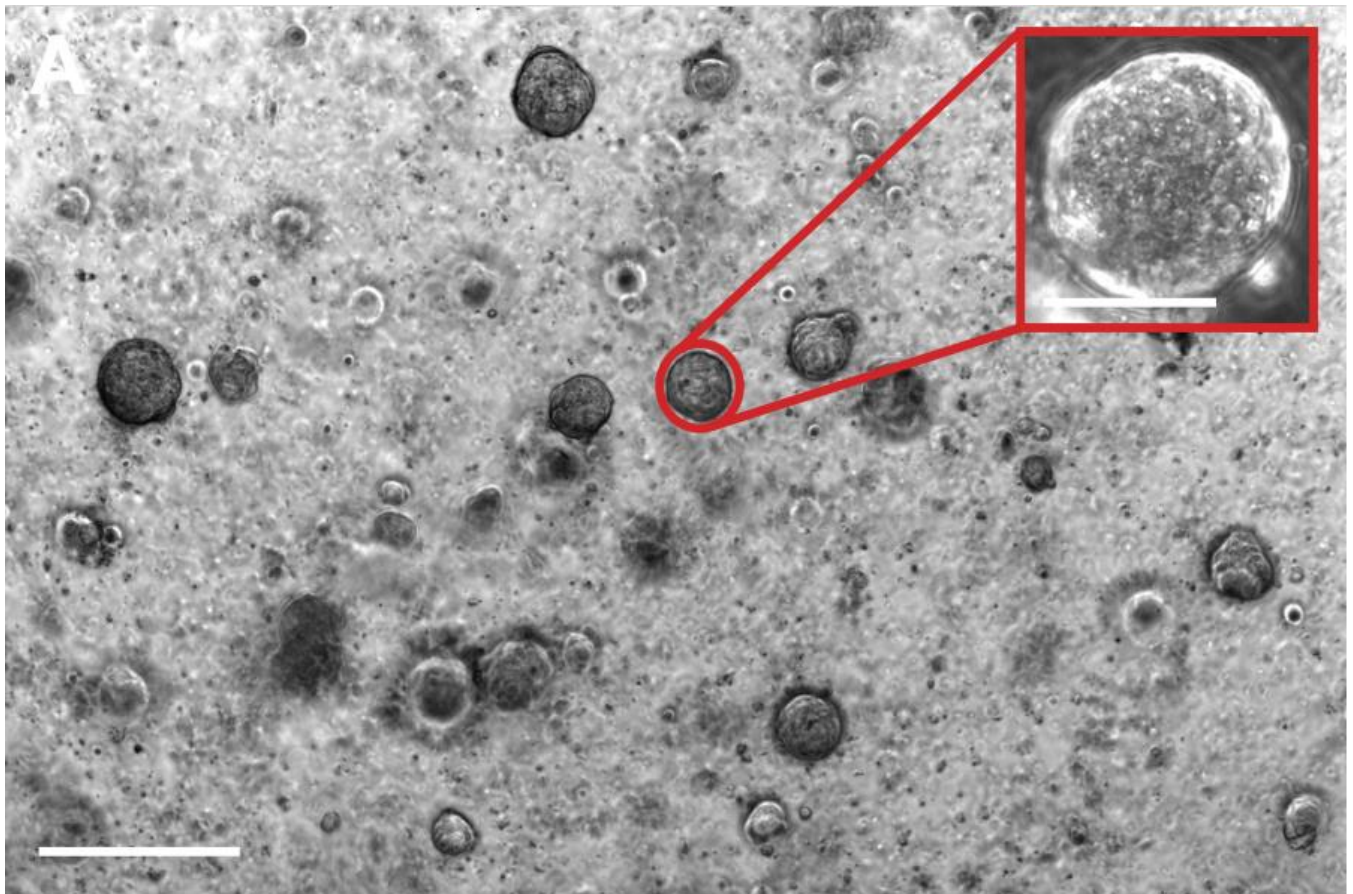


Figure 6. Patient-derived organoids. Transmitted light microscopy, magnification 4x. Scale bar equals 250 μm . Insets: phase contrast microscopy, 20x magnification. (A) Organoids derived from radical prostatectomy tissue from prostate tumor with Gleason Score 5+4. Day 13. Inset scale bar equals 50 μm . (B) Organoids derived from video-assisted thoracoscopic surgery of a metastatic rectal tumor protruding from the sternum. Day 25. Inset: Lung organoid. Inset scale bar equals 200 μm .

Microtubule tip motion analysis

Fluorescent comets form at the polymerizing ends of MTs when the end-binding protein 1 (EB1) is GFP-labeled and allow for direct measurements of MT tip dynamics in living cells (Matov et al., 2010). Harvesting EB1 data allows for the generation of large, statistically comprehensive datasets in which for every cell we can measure over 38,000 data points (Fig. 7). In cell lines, we analyze 10 to 20 cells (i.e., between $\frac{1}{2}$ and 1 million quantitative readouts, see Vid. 1 and Vid. 2 for examples) per condition to evaluate drug susceptibility at very low drug doses by measuring the specific patterns of changes in MT dynamics (Matov, 2024e). In patient-derived organoids, it is difficult to know the genetic and epigenetic make-up of the cells in an organoid, in particular in primary, drug-naïve tumors. We performed EB1 comet analysis in organoid cells (Vid. 3) from four metastatic castrate-resistant prostate tumors, which showed correlation between MT dynamics and gene expression of MT-regulators (Matov, 2025a), and our predictions regarding drug resistance can be validated in a clinical trial.

A plethora of the cellular proteins exhibit ambiguity in function and response to perturbations. There exists a high level of regional variability in the dynamics of polymer networks in living cells, which are considerably more interdigitated than initially perceived and reported in the literature. Drugs bind to proteins within these networks and affect their function. Consequentially, the modulation of MT and F-actin dynamics inevitably affects drug efficacy. Answers about the potential efficacy of a drug can, thus, be obtained by utilizing clinical software systems that measure, in great detail, the effects of a regimen on its cellular targets. Molecular manipulations of living patient-derived cells *ex vivo* can reveal which secondary mechanism would be activated after a particular intervention.

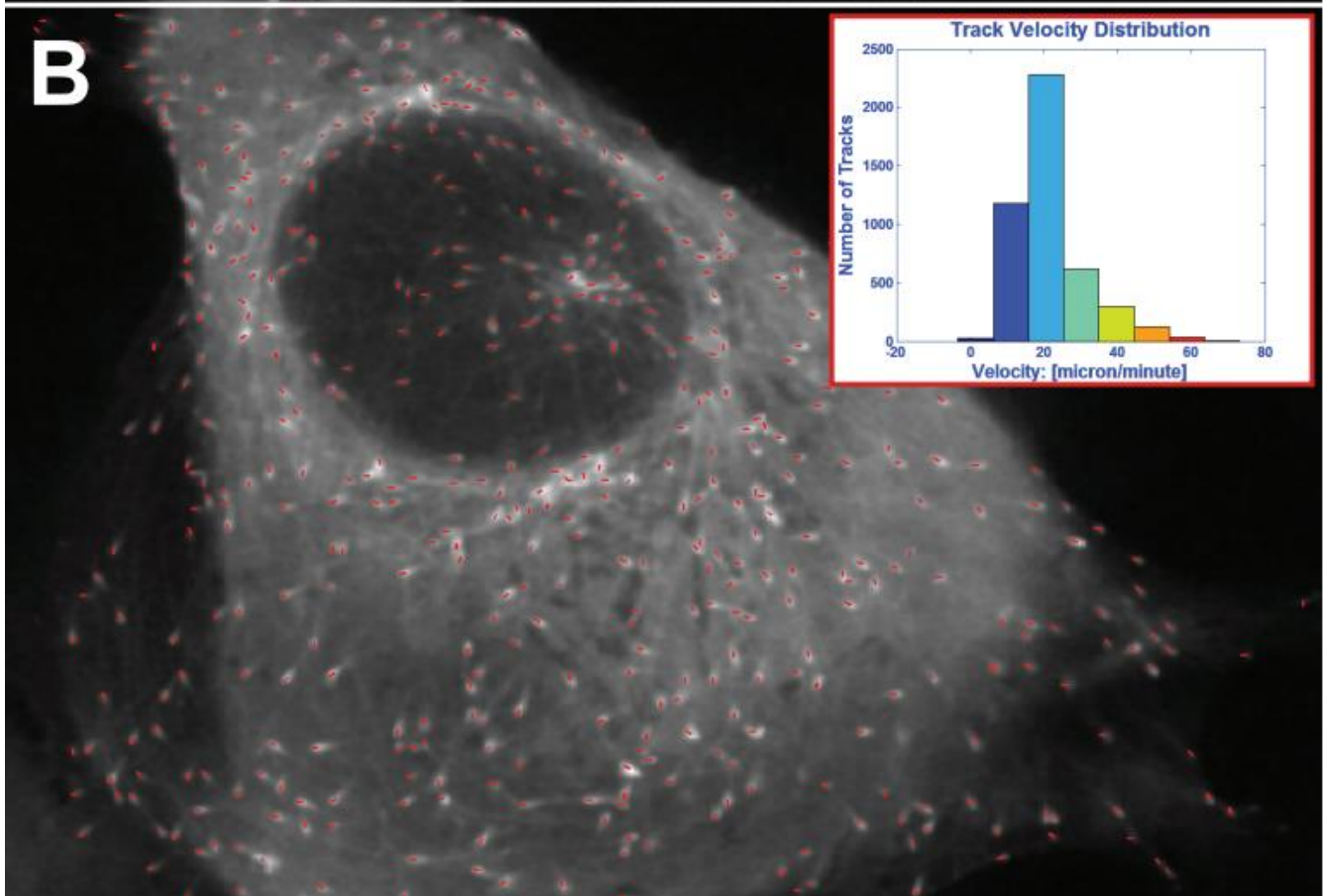
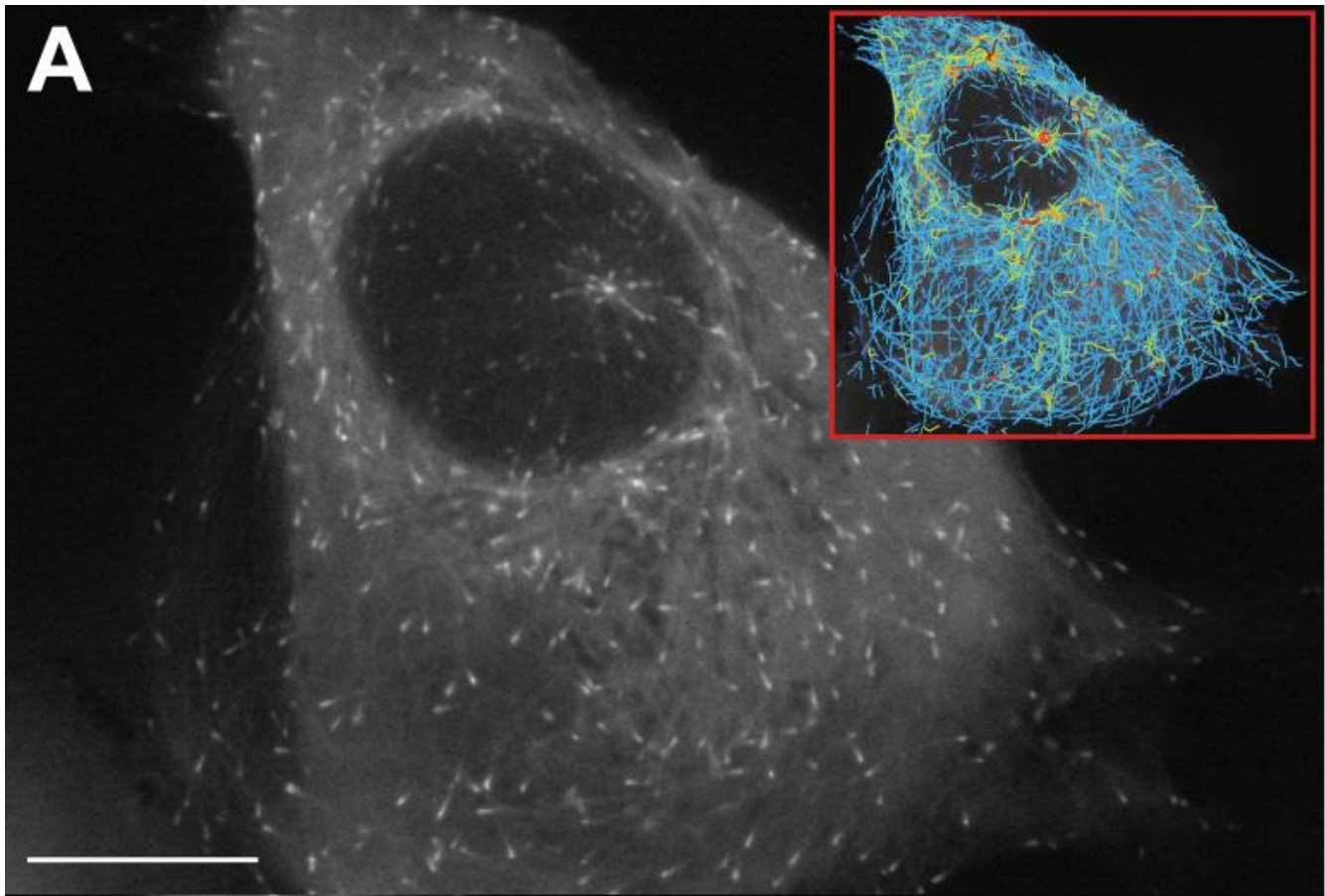


Figure 7. EB1 comets detection and motion tracking in MDA-MB-231 breast cancer cells. (A) MT tips are labeled with EB1 Δ C-2xEGFP, imaged for a minute with an acquisition rate of two images per second. (B) EB1 comets formed at the tips of polymerizing MTs are detected (Matov et al., 2011) and computationally tracked (Yang et al., 2005). The upper inset displays an overlay with the EB1 trajectories for comets persisting in at least four image frames, i.e., at least 1.5 seconds. The lower inset shows the histogram of EB1 speed probability density function of these trajectories, which comprise over 38,000 comets. The average speed is 24.4 ± 9.4 $\mu\text{m}/\text{min}$. The maximal EB1 speed is over 70 $\mu\text{m}/\text{min}$. The speed distribution is unimodal. The color-coding represents EB1 speeds and colder colors correspond to lower speeds, and warmer colors correspond to faster speeds. Scale bar equals 10 μm .

Such clinical research can aid the discovery of an optimal drug selection for each disease, which is the motivation to translating all image analysis of molecular markers from off-line software to real-time algorithms.

Validation of drug susceptibility in patient cells

In prostate cancer organoids derived from intraductal carcinoma, an aggressive type of adenocarcinoma with very particular glandular organoids in primary samples (Matov, 2024f), we measured attenuated MT polymerization rates in comparison to other metastatic tumors (Matov, 2025a). In the intraductal carcinoma organoids, the MT-associated protein 2 (MAP2) was upregulated up to 23-fold in comparison to the other tumors. MAP2/Tau stabilizes MTs by attenuating the polymerization rates by binding along the lattice (Al-Bassam et al., 2002), which are the changes we directly measured with our computer vision assay (Matov, 2025a). Such datasets can be validated with patient samples, such as urinary microRNAs (miRs).

Non-invasive, for instance from urine samples, or minimally-invasive methods for obtaining patient cells allow to monitor disease progression and patient response to treatment throughout the course of a clinical trial. We can transduce cells and label proteins of interest overnight and, depending on the disease and drugs used, tests can be carried out as soon as a few hours after sample collection. Having the ability to test a number of drugs and combinations *ex vivo* will be critical in the treatment of

pathologies for which there is no known cure. Once the specific impaired molecular mechanisms is identified for the particular patient, treatment options which correct the aberrations can be selected. This way, we can transform patient treatment.

We analyzed urine samples from 15 healthy individuals and 13 drug-naïve stage IV lung cancer patients and detected 947 miRs, 20 of which could be used to discriminate healthy from lung cancer samples (Matov, 2024i). The biomarkers were detected are implicated in cellular functions, such as cell proliferation, which is directly linked to MT dynamics. miR-577 inhibits cell proliferation and invasion in non-small cell lung cancer (NSCLC) (Men et al., 2019). miR-141-3p reduces pulmonary hypoxia / reoxygenation injury (Zhan et al., 2024). miR-29c-3p is significantly decreased in the plasma of lung cancer patients and can be used as a biomarker discriminating between NSCLC and small cell lung cancer (SCLC) (Zhang et al., 2023). miR-95-3p inhibits the invasiveness of metastatic lung cancer through downregulation of cyclin D1 (Hwang et al., 2015). miR-335-5p is significantly decreased in parenchymal lung fibroblasts of smokers (Ong et al., 2019). miR-29a-3p prevents NSCLC tumor growth and cell proliferation, migration, and invasion by inhibiting the Wnt/ β -catenin signaling pathway (Zhang et al., 2022). miR-532-3p inhibits metastasis and proliferation of NSCLC by targeting FOXP3 (Ni et al., 2021). There are other examples of urinary biomarkers, which can be validated in data from primary tumor tissues and plasma samples. Overall, the utilization of longitudinal urine samples will allow a clinical validation of predictions regarding drug treatment established in organoids by analysis of exosomes (Matov, 2024a) and the miRs they contain (Fig. 8).

Computational analyses of gene expression of MT-regulators in patient cells can provide hypotheses regarding drug efficacy, which can be validated by the combined utilization of a live-cell computer vision and sequencing of miRs. This three-pronged approach will allow us to select an effective drug regimen, for example in immunotherapy. The MTs are involved in the formation of the immunological

synapse and taxane therapy affects the immune system, and tubulin inhibitors might synergize with the immune cells under the right conditions. The links between systemic therapy with tubulin inhibitors and immunotherapy in the context of the regulation of MTs and other cytoskeletal proteins seem of key importance for the success of immune cells in killing tumor cells of epithelial origin. For these reasons, we propose computational assays to anticipate drug resistance and facilitate the selection of an optimal drug regimen in oncology.

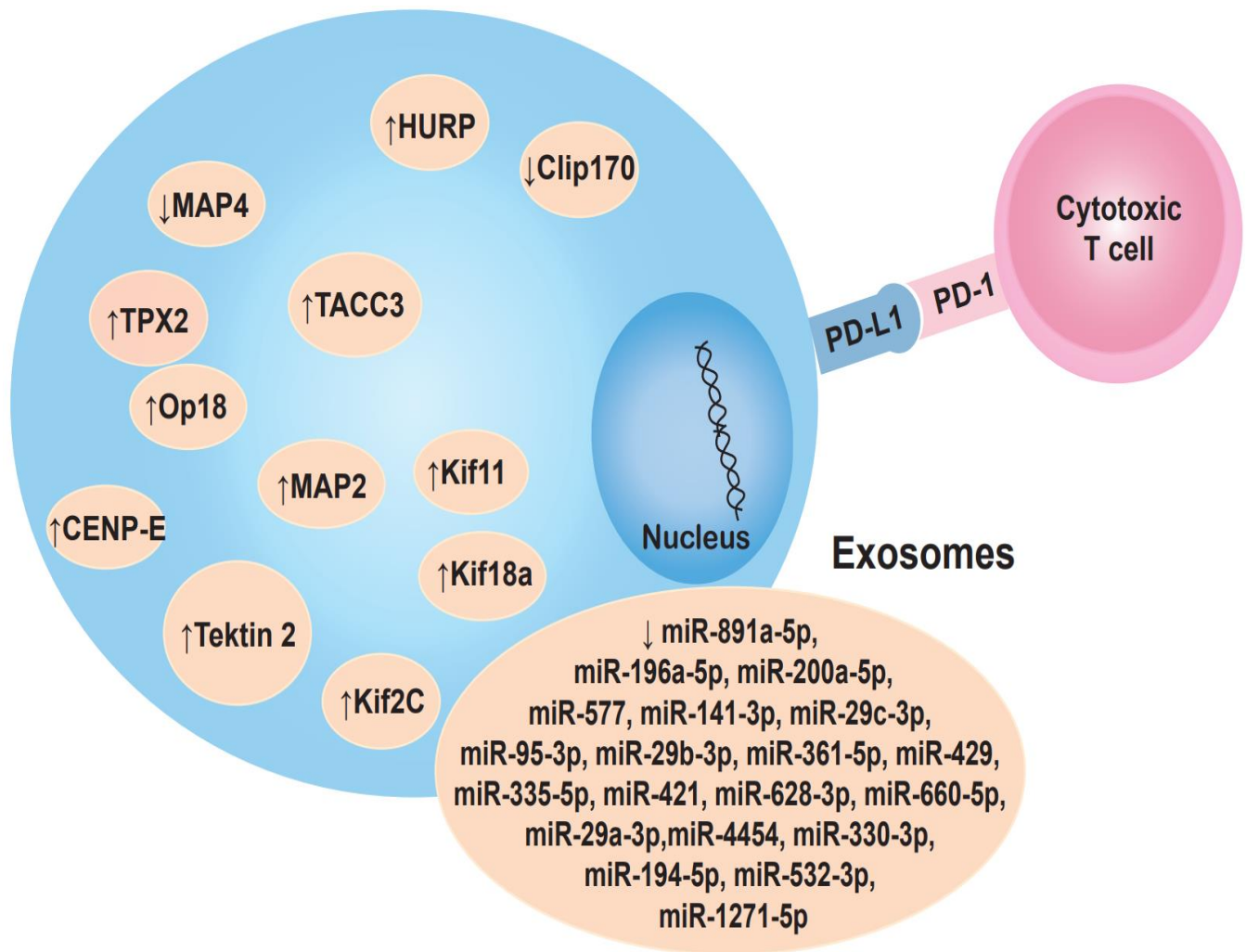


Figure 8. Dysregulation in patient samples. The figure presents novel urinary miR biomarkers in lung cancer (Matov, 2024f; Matov, 2024i) and a pattern of dysregulated genes we identified in intraductal prostate cancer (Matov, 2025a). In addition to genetic sequencing, computer vision analysis of exosomes (see Vid. 4) can validate the drug resistance mechanisms.

Microtubule dynamics regulation of immune response

EB1 interacts with T cell receptor cytosolic regions and mediates the organization of an immunological synapse to transduce activation signals (Lasserre and Alcover, 2012). Lytic granules from cytotoxic T cells have been shown to exhibit kinesin-dependent motility on MTs (Burkhardt et al., 1993). T cell activation and function can, therefore, be evaluated in terms of reorganization and modulation of the cytoskeleton (Matov, 2024f; Matov, 2024g; Matov and Bacconi, 2024; Matov and Danuser, 2004; Ponti et al., 2003) and the EB1 comet metrics will be validated by the levels of measured cytokine production. After validation and calibration, the software can be utilized for the discovery of novel drug combinations that allow personalized treatment.

We derived a prostate cancer organoid from micro-metastasis at a retroperitoneal lymph node for which whole genome sequencing showed homozygous mutations in *PTEN* and *BRCA2* as well as mutated *KIF4B* (Matov, 2024f). When prostate tumors escape the capsule, they form micro-metastatic lesions at the retroperitoneal lymph nodes. In our organoid culture, such drug-naïve tumors formed slow-proliferating tumors and had driver mutations, such as homozygous mutations in *PTEN* (exon2, c.G194>C, p.C65S) and *BRCA2* (exon14, c.T7397>C, p.V2466A) (Matov, 2025b). A heterozygous mutation in *KIF4B* (exon1, c.G1739>T, p.R580L) likely contributes to errors during chromosome segregation. We detected also androgen receptor deletion, which we have shown to be associated with smaller tumor cells and more aggressive disease (Matov, 2024c; Matov, 2024d). Overall, image analysis in living cells can validate the mechanisms suggested by sequencing data and thus inform therapy.

Cell therapy is becoming the forefront of precision medicine, and it would be critical to be able to anticipate the mechanisms of action of the engineered immune cells. Natural killer cells and cytotoxic T cells employ different mechanisms to kill their targets, for instance by secreting cytotoxic lysosomes using the MT cytoskeleton for trafficking and release. There is also a plethora of effects induced in the

target cells, most well-studied of which lead to apoptosis and ferroptosis (Viswanathan et al., 2017), a recently identified potent, caspase-independent, mechanism of programmed cell death. The exact pathways activated during therapy can be pinpointed by measuring its effects on the target proteins in patient-derived living cells *ex vivo*.

It is conceivable that for different patients, with overall very similar genetic profiles, a distinct type of engineered immune cells will be required. Given the availability of high-quality fundamental research equipment for high resolution live-cell microscopy in most university hospitals, what we propose is to embed in these systems such real-time software for automated quantification and on-the-fly statistical analysis of intracellular behavior. Introducing this quantitative imaging method to the clinic will allow physicians to fine-tune, with a high level of certainty, an optimal treatment regimen for each patient.

Analysis of fundus fluorescence

Neurodegenerative diseases are challenging to diagnose and stage. As an extension of the central nervous system, the eye harbors retina ganglion cells vulnerable to degeneration, and the fundus exhibits symptoms of early manifestations of amyloid protein aggregation linked to neurodegeneration. The diagnosis of patients having a disease associated with protein aggregation could be based on capturing fundus auto-fluorescence (AF) images of the retina, but such baseline images have low contrast and high signal-to-noise ratio. We performed analysis in fundus AF image datasets obtained from non-human primates with automated detection algorithms, such as difference of Gaussians (Matov, 2024b) and stationary wavelet transform (Olivo-Marin, 2002). The largest baseline AF puncta (Fig. 9) detected had a peak intensity of 15.7% of the maximal intensity in the image and a perimeter (length of the boundary) of 200 μm , which indicates a utility of methodology for enhanced fluorescence emission.

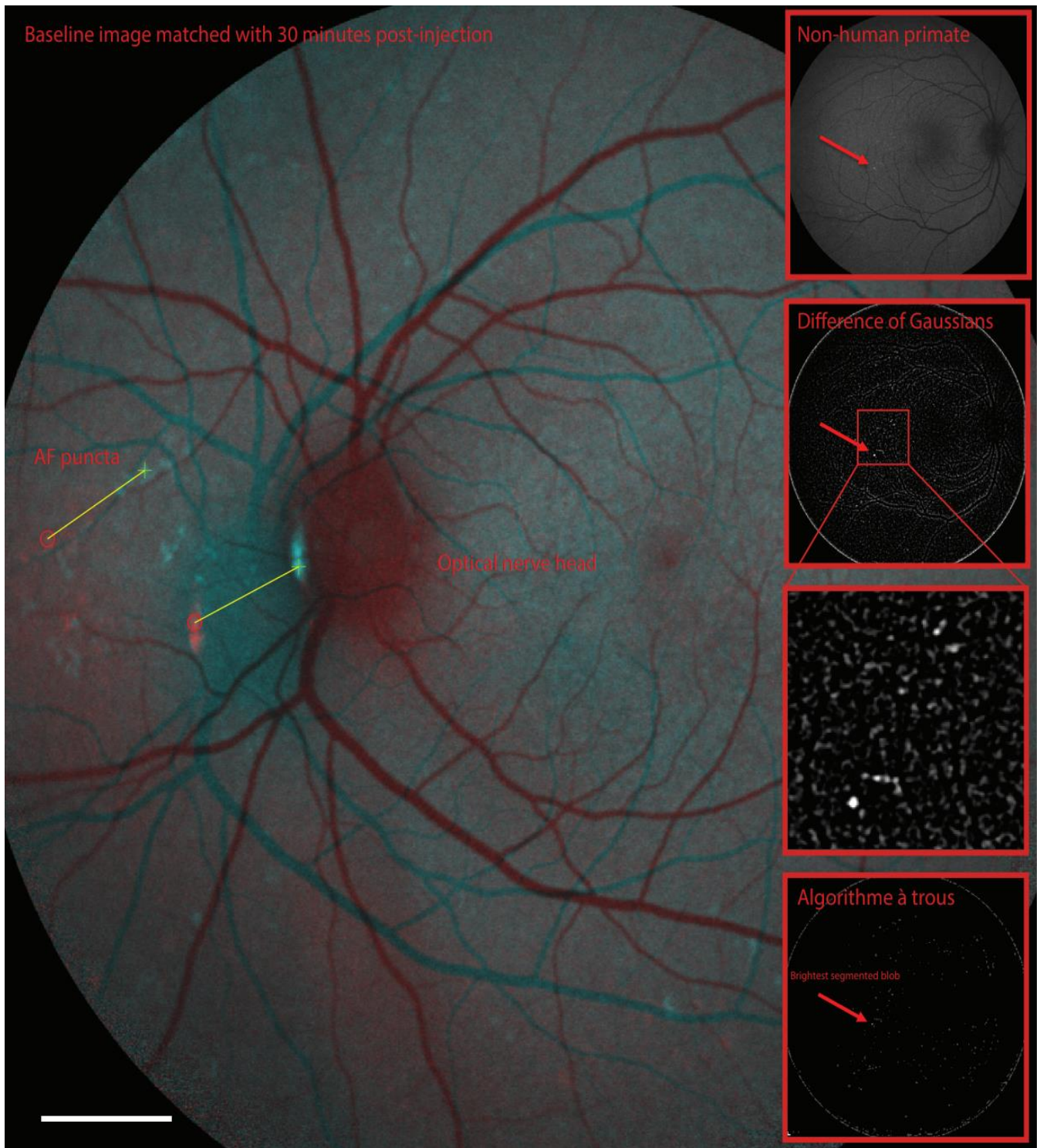


Figure 9. Eye fundus with matched auto-fluorescence at baseline and hyper-fluorescent puncta 30 minutes post injection of a fluorescence emitting dye. *In vivo* imaging of fundus of the eye in two time-frames, including prior to injection and 30 minutes post injection (Pilotte et al., 2024). AF and hyper-fluorescent puncta are indicative of disease. We show matching of two puncta, one in the area of the optical nerve head and another in the retina, which shows neurodegeneration. Matching was done with SURF (Bay et al., 2008). Inset images show another example of fundus fluorescence imaging and the detection of AF puncta with a band-pass filter (difference of Gaussians) (Matov et al., 2011) and stationary wavelet transform (algorithme à trous) (Olivo-Marin, 2002). The automatically selected area was the brightest segmented blob after image transformation. Scale bar equals 2 mm.

An amyloid-binding fluorophore can enhance fundus imaging (Aguilar-Calvo et al., 2022; Pilotte et al., 2024; Pilotte et al., 2025) and aid the analysis of amyloid deposits. Computer vision analysis of compounds that emit fundus fluorescence upon binding to a misfolded or aggregated protein can facilitate the diagnosis of Alzheimer's disease, cerebral amyloid angiopathy, traumatic brain injury, glaucoma, age-related macular degeneration, Parkinson's disease, multiple system atrophy, dementia with Lewy bodies, amyotrophic lateral sclerosis, and a dozen others. Immediately after injection, the dye enters the retina (about 15 seconds post-injection) and fills the retinal vasculature rapidly. Figure 9 shows matching of two AF puncta, one in the area of the optical nerve head and another in the retina, with hyper-fluorescent signals 30 minutes after injection with a fluorescent emitting dye binding to misfolded or aggregated proteins by applying a SURF detector (Bay et al., 2008) (see Materials and Methods). The *in vivo* analysis of fundus fluorescence also faces a challenge in the continuous 3D rotation of the eye during image acquisition. In this context, a real-time image registration and segmentation software will facilitate the analysis of fundus fluorescence puncta.

DataSet Tracker

All degenerative diseases are associated with impairment in intracellular trafficking. The highly dynamic organization and remodeling of the cellular cytoskeleton are dysfunctional in pathology and often lead to drug resistance. Successful analyses of the mechanism of drug action require statistical analysis of large-scale readouts of molecular interactions. Our objective has been to develop resources for functional interrogation of drug response in a physiologically relevant system amenable to molecular manipulations and investigate personalized drug response *ex vivo*. We have developed image analysis software for automated motion tracking of labeled MTs and filamentous actin – ClusterTrack (Matov et al., 2010) (for measurements of interphase cells) and Instantaneous Flow Tracking Algorithm (IFTA) (Matov, 2024b; Matov et al., 2011) (for measurements of interdigitated flows in dividing cells, contractile filamentous actin meshworks in migrating epithelial cells and growth cones) – and other

biomedical computer vision software packages (Matov, 2024g). We have used IFTA to constrain the Kalman filter with information of spatio-temporal gradients in the instantaneous flow behaviors, which increased the Kalman tracking success rate from 61% to 96% (Fig. 10).

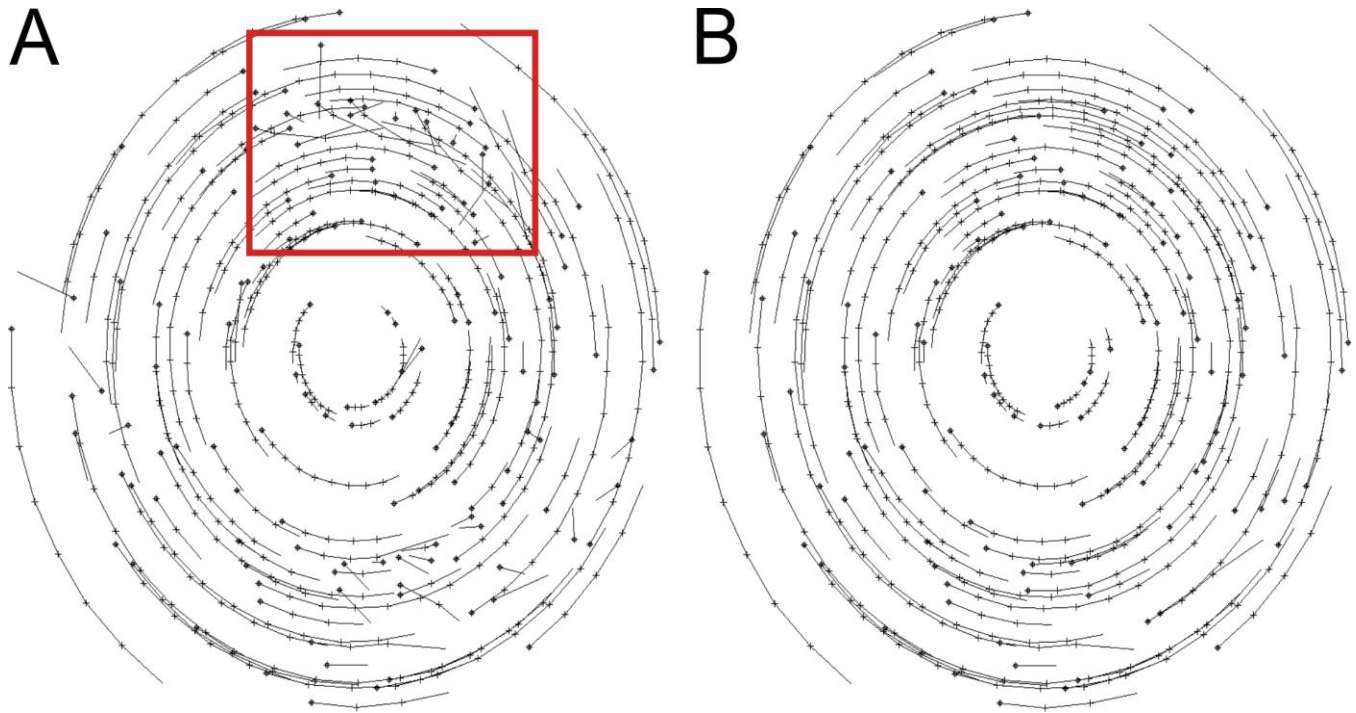


Figure 10. Tracking the motion of synthetic markers in time-lapse image series. The figure (adapted from (Yang et al., 2005)) presents the changes in Kalman filtering tracking results when a flow constraint based on IFTA is imposed during tracking in the rotating dish sequence, consisting of 10 frames with 80 seeds each. Figure legend: A square marks a trajectory starting point, a cross marks the selected for the trajectory feature in the next time-frame. (A) Tracking results without IFTA flow constraint. Success rate: 61.1%. Red square highlights an area with multiple wrong links. (B) Tracking results with flow constraint. Imposing IFTA flow constraints improves the tracking success rate to 96.0%.

All quantitative imaging examples presented here will benefit from having the analysis results displayed on the microscope screen on-the-fly during sample observation and image acquisition. In this context, the manuscript explores, for the first time, a real-time quantitative way to analyze the changes occurring in the cell. In an effort to improve the efficiency in drug development and efficacy evaluation, we have developed a real-time computer vision software, which connects to the microscope camera, processes multiple image frames per second (five frames per second for the example in Fig. 11 – see lower right

corner of the image and Vid. 5), and instantly displays and stores statistical readouts in parallel to sample observation and image acquisition.

Our objective is to offer a tool not only capable to anticipate drug resistance for existing regimens, but also methodology that can be seamlessly applied in the identification of putative molecular targets during drug discovery. Quantifying with ease the morphological, localization and other dynamical changes in patient cells can certainly help clinical decisions and support timely changes in the original course of treatment by providing feedback and evidence for treatment efficacy, or the lack thereof, in real time. It will also advance our understanding of the regulation of the cells comprising our organs and tissues in normal physiology and in disease.

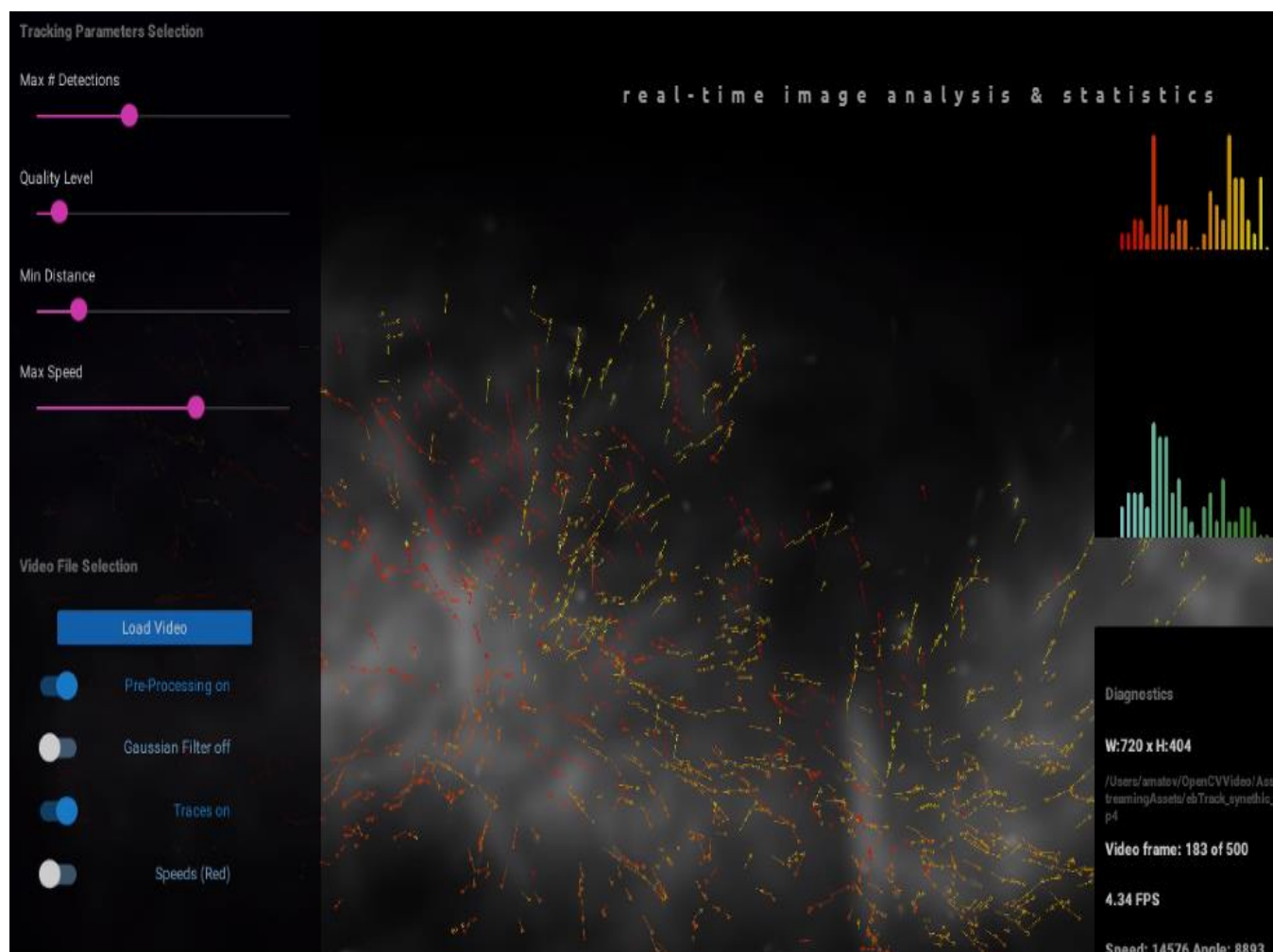


Figure 11. Real-time tracking the motion of synthetic markers in time-lapse image series. The figure presents novel software (a demo video of this package is available for viewing at datasetanalysis.com/synthetic-demo) developed with the gaming engine of Unity Technologies. The figure shows computer vision analysis of the motion of synthetic markers, which mimic live-cell fluorescent microscopy image sequences. Displacement vectors color-coding is used to show the angular direction as well as the speed of motion. A button selection allows changing the display preferences. On the figure, yellow vectors move to the right and are also shown in yellow within the right peak of the bi-modal histogram. Similarly, the vectors moving to the left are in red, both on the image overlay and within the left peak of the bi-modal histogram in the upper right corner of the screen. The second display option (not shown) changes the displacement vectors color-coding to showing different shades of green, depending on the speed. Observe on the unimodal histogram to the right that most of the features move slowly (the light-green peak to the left), while a few features move very fast (the dark-green distribution tail on the right side). Real-time information on the frames per second analyzed, the average values for the speed, and the angular vector orientations are displayed in the lower right corner of the screen. On the left side of the screen, there are sliders in the upper left corner, which allow to set the (i) the upper limit for the number of detected features based on the a priori knowledge of the nature of the motion in the analyzed sample, (ii) the level of statistical significance for the feature selection step, i.e., the level of feature detection stringency, (iii) the minimum distance between features, which is another parameter selection done based on a priori knowledge of the type of sample analyzed, and (iv) a cut-off for the feature search radius, which limits the maximal allowed displacement; this is another parameter, which is selected based on the knowledge of the sample. By providing sample-specific input to the tracking module, the parameters selection allows to limit the computational complexity, to minimize the tracking errors, and to deliver the fastest analysis results. The blue buttons in the lower-left corner of the screen allow to change various aspects of the screen display in terms of showing image segmentation or motion tracking results, single-segment tracks (between just two frames) or the aggregated trajectories and, as described above, the vector color-coding (angles in red/yellow vs. speeds in different shades of green). See Materials and Methods for information on how to download and test the software. We will extend the current real-time 2D functionality to 3D analysis using artificial intelligence algorithms.

Algorithm for real-time optical tracking

We developed our novel software package (a demo video of this package is available for viewing at datasetanalysis.com/synthetic-demo) with the gaming engine of Unity Technologies (Unity, 2017). The engine supports desktop, mobile, console, augmented reality, and virtual reality platforms. It is convenient for iOS and Android mobile applications development. We will extend the current real-time 2D functionality to 3D analysis using AI algorithms.

Figure 11 shows computer vision analysis of the motion of synthetic markers, which mimic live-cell fluorescent microscopy image sequences. Displacement vectors color-coding is used to show the angular direction as well as the speed of motion. A button selection allows changing the display preferences. We have displayed a color-coding that gradually changes the color from yellow to red as vectors change their angular orientation from 90° to the right to 90° to the left, i.e., features moving upwards are color-coded in orange, accordingly. In this example, yellow vectors that move to the right and are shown as

the right peak of the distribution in yellow of the bi-modal histogram. Similarly, the vectors moving to the left are in red, both on the image overlay and within the left peak of the bi-modal histogram in the upper right corner of the screen. The second display option (only shown as a histogram) changes the displacement vectors color-coding to showing different shades of green, depending on the speed, with slow moving features are shown in light blue and the color is gradually changing toward green as the speed increases (right side of the histogram). Observe on the unimodal histogram to the right showing that most of the features move slower (the light-green peak to the left), while a few features move very fast (the dark-green distribution tail on the right side). Real-time information on the frames per second analyzed, the average values for the speed, and the angular vector orientations are displayed in the lower right corner of the screen.

On the left side of the screen, there are sliders for selection of analysis parameters in the upper left corner, which allow to set the (i) the upper limit for the number of detected features based on the a priori knowledge of the limits in the motion in the analyzed sample, (ii) the level of statistical significance for the feature selection step, i.e., the level of feature detection stringency, (iii) the minimum distance between features, which is another parameter selection done based on a priori knowledge of the type of sample analyzed, and (iv) a cut-off for the feature search radius, which limits the maximal allowed displacement; this is another parameter, which is selected based on a priori knowledge of the sample. By providing sample-specific input to the tracking module, the parameters selection allows to limit the computational complexity, to minimize the tracking errors, and to deliver the fastest analysis results. The blue buttons in the lower-left corner of the screen allow to change various aspects of the screen display in terms of showing image segmentation or motion tracking results, single-segment tracks (between just two frames) or the aggregated trajectories as the video progresses and, as described above, the vector color-coding (angles in red/yellow vs. speeds in different shades of blue/green).

For the purposes of demonstrating the workings of our real-time analysis software, we have generated synthetic videos displaying the radial motion of fluorescent features originating from two distinct focal points (Fig. 11, Vid. 5). In this contribution, we pre-process images making up the video and select features for motion tracking on-the-fly as the video file is loaded into the software. For each feature type, we will extract a set of distinctive key features, identify descriptor vectors of the features, and compute motion metrics to distinguish between drug-resistant and drug-sensitive profiles in cells derived from patients and elucidate mechanisms of resistance. This quantitative analysis (Vid. 6, Vid. 7) will, therefore, allow for the identification of the key signaling pathways involved in resistance, which may contribute to the personalization of the drug treatment regimen and the functional testing of novel compounds. Our approach will allow evaluating the relative contribution of different signaling pathways in drug response in disease cells originating from different organs and tissues.

Our preliminary software development uses a 2D tracking strategy in which we utilize three steps performed by well-established algorithms implemented as real-time robotics libraries by OpenCV (Bradski, 2000; Pulli et al., 2012). In brief, images making up the video are pre-processed or de-noised by a specialized background subtraction method (Zivkovic, 2004; Zivkovic, 2006). The algorithm aggregates statistical representation of the intensity profile for each pixel over time during live camera operation by the use of Gaussian (de Moivre, 1718) mixture models (Duda and Hart, 1973) in which the number of Gaussian function components is recursively updated with every new image. Lagrange multipliers (Lagrange, 1788) are introduced in the estimation of the maximum likelihood (Fisher, 1912) to determine the number of components. The influence of previous images in computing the distributions for each pixel is exponentially decaying with time. For multinomial distributions, a conjugate prior is utilized based on a Dirichlet distribution (Dirichlet, 1839) related to the minimum message length criterion (Wallace and Boulton, 1968).

Next, a watershed-based algorithm was used to select the features for tracking (Shi and Tomasi, 1994). The algorithm monitors the quality of the features during tracking by estimating feature dissimilarity between the first and current frames. The section procedure evaluates feature texturedness as it relates to the tracking accuracy. To optimize the tracking accuracy, metrics for two motion models for affine image changes (linear warping) and translation, are computed by Newton-Raphson (Wallis, 1685) minimization. Translation is the better metric when the inter-frame camera translation is small, while affine changes are important for determining dissimilarity between distant frames. The method successfully detects feature occlusions and disocclusions, and selects features based on a threshold for the smaller eigenvalue of the deformation and displacement matrix.

Lastly, the Lucas-Kanade optical flow algorithm, which has been cited some 20,000 times, was used for motion tracking (Lucas and Kanade, 1981). It is an image registration technique that utilizes spatial Gauss-Newton (Gauss, 1809) gradient descent non-linear optimization to direct the search for the feature that yields the best match. While a brute force approach would require quadratic complexity related to the dimensions of the feature, this method is linear in the number of pixels examined in the feature. An initial estimation of the disparity vector is updated via a Newton-Raphson iteration until convergence. The optical flow regression is done via computation of least squares (Legendre, 1805) with pixel weights based on a Gaussian function at the central pixel of the feature. The approach can handle feature rotation, scaling, and shearing.

The development environment we used was of the cross-platform game engine of Unity Technologies Inc. We compiled and tested our software on multiple platforms, such as Windows PC, Macintosh computer, iPhone smartphone, Android smartphone, and Microsoft HoloLens smart glasses. See Materials and Methods on how to download and test the software.

Examples of real-time analysis

A key novelty is that our computational platform outputs results in real-time, in parallel to image acquisition, which facilitates and speeds up research and clinical efforts by delivering instant visualization of data analysis and statistical outcomes. Such approach offers a clear improvement on the selection of imaging parameters and drug concentrations empirically by offering precise quantification of changes in the dynamics of the underlying cellular processes. We present the functionality of our software with videos demonstrating specific features. Video 8 shows motion tracking of fluorescently labeled MT ends to measure polymerization rates in an epithelial cell. To compare subcellular differences in regulation, we have introduced the selection of a region of interest (ROI), shown as a red rectangle. Video 9 shows similar analysis, but with histograms for MT polymerization rates (lower histogram) and for angular orientation of the MTs (upper histogram). The graphics are overlaid on the original images and can be displayed as augmented reality overlay in real time.

Video 10 shows glioblastoma multiforme tumor-propagating cells imaged with fluorescently labeled histone H3K9me3 marker, which we have tracked. Our analysis, which processed 19 frames per second, was focused on determining nuclear reorganization in glia cells after drug treatment to reverse differentiation. Vectors with different shades of red show the angular orientation of the nuclear marks. Vectors with different shades of blue show their speeds of motion, where lighter blue represents slower speeds.

Video 11 shows an example of our phone app, which captures the motion when being pointed at a computer screen. The video shows the functionality during software development when the image dataset was used to calibrate the different modules of the software. Modules can be added and customized, depending on the application. Video 12 shows another example of our phone app, which captures the motion when being pointed at a computer screen. On the video molecular marker in cellular

proteins encapsulated in a microfluidic droplet are being detected and tracked in real time. The tags appearing next to each protein in real time can either display the speed or angle of motion, or indicate the identity number of each MT.

Real-time motion tracking with transformers

To extend the current functionality into obtaining the full trajectories, we will utilize the vectors obtained in each frame, together with the associated information on feature intensity and morphology, to generate embeddings (Vaswani et al., 2017) for a generative transformer network in which the tokens are the spatial coordinates of the features we track. This will allow training of the network to associate the most likely next feature in an image sequence, similar to the way large language models generate text. Further, we will retrain a transformer network with a new set of tokens - with lists of 2D or 3D coordinates rather than words and with trajectories (lists of linked coordinates) rather than sentences of human speech, i.e., we will retrain a large language model with motion trajectory data. We have generated several thousand time-lapse microscopy movies with about 2-10,000 trajectories consisting of about 3-20 features (either MT end-binding proteins or fluorescent speckles) linked in each trajectory (Brennan et al., 2008; Galletti et al., 2014; Gatlin et al., 2010; Gatlin et al., 2009; Harkcom et al., 2014; Matov, 2024c; Matov, 2024e; Matov et al., 2010; Matov and Bacconi, 2024; Matov et al., 2016; Matov et al., 2015; Thoma et al., 2010). These are about 60 million data points, but many more existing movies/data can be obtained from our academic collaborators. As we have pre-processed the data, the preliminary computer vision analysis has already been done and the results have been validated and published, which will facilitate the training and benchmarking.

Disease classification with reinforcement learning

One way to approach the classification of new patient samples is to utilize mathematical reasoning based on a large reasoning model (LRM) and reinforcement learning (RL) is utilized for post-training of

LLMs. Reasoning or a thought process consists of a sequence of tokens representing the steps in the reasoning trajectories. A Kullback-Leibler divergence constraint can achieve good empirical results on a range of challenging policy learning tasks (Schulman et al., 2015). The addition of a Group Relative Policy Optimization (GRPO) (Shao et al., 2024), a modification of the RL algorithm for Proximal Policy Optimization (Schulman et al., 2017), reduces the requirements for training data. For each new sample, GRPO samples a group of outputs from the old policy and then optimizes the policy model by maximizing the objective function, which is the expectation for the average reward of multiple sampled outputs, produced in response to the same question as the baseline. It utilizes a penalty based on the computing the Monte-Carlo approximations of the Kullback-Leibler divergence between the policy model and the reference model.

DISCUSSION

Reinforcement learning techniques, such as Markov Decision Processes (Kakade and Langford, 2002; Schneider and Wagner, 1957), can provide the basis for sample stratification based on policies for sample classification in oncology as well as neurodegeneration. In particular, fluid intelligence (Cattell, 1943) applications of LRMs that depend on no prior training data can be useful in identifying and diagnosing new clinical conditions in real time. This context is important because many current disease types appear to be multiple diseases wrongly classified as one. The ability to distinguish different distinct clinical features will improve the precision of the treatment plans. Most misdiagnosed cases are the result of considering superficial clinical information in which indicators for different conditions happen to overlap. Without distinct markers, the diagnosis is made based on the highest probability, given incomplete information and the historical data – which systematically undermines the statistical representation of some diseases to the point of considering them as rare diseases.

Quantitative cell biological profiling of subcellular interactions in disease is required to understand the mechanisms of pathogenesis and elucidate the mechanisms of drug action. During pathogenesis, or due to drug treatment in disease, cells change their intracellular organization, rearrange their internal components as they grow, divide, and adapt mechanically to a hostile environment. These functions depend on proteins, cytoskeletal filaments, and focal adhesion complexes, which provide the cell shape and its capacity for directed movement. The integration of measurements of intracellular dynamics and the contribution of multiple genetic pathways in degenerative diseases is vital for the development of biomarkers for the early detection of pathogenesis and therapy efficacy. Methods that can reliably analyze the evolution of the morphology and localization of cellular proteins over hundreds of time-lapse frames will be very relevant for capturing the changes in the subcellular organization in disease and during treatment. They will allow physicians to compare visually and quantitatively the effects of treatment regimens and select the one most likely to be efficacious.

Tumor growth curves can be quantified using mathematical models, such as the Gometz function (Gompertz, 1825; Winsor, 1932). Heuristic analysis (Jungius, 1622) brought sigmoid growth kinetics into the arena of cancer therapeutics by establishing the observation that a given administration of cancer therapy killed a specific fraction of the cancer cells present rather than an absolute number (Skipper et al., 1964). This observation inherently leads to the conclusion that acquired drug resistance is inevitable. Emerging evidence implicates nonmutational mechanisms, including changes in cell state during the early stages of acquired drug resistance. Targeting nonmutational resistance may, therefore, present a therapeutic opportunity to eliminate residual surviving tumor cells and impede relapse (Hangauer et al., 2017).

The integration of measurements of intracellular dynamics and the contribution of multiple genetic pathways in degenerative diseases is vital for the development of biomarkers for the early detection of

pathogenesis and therapy efficacy. We developed a software suite (DataSet Tracker) for real-time analysis designed to run on PCs, Macs, smartphones, and smart glasses and suitable for resource-constrained, on-the-fly computing in microscopes without internet connectivity; a demo is available for viewing at datasetanalysis.com. Our objective has been to present the community with an integrated, easy to use by all, tool for resolving the complex cytoskeletal dynamics and it is our goal to have such software system approved for use in the clinical practice. A key novelty is that our computational platform outputs results in real-time, during imaging and without having to store the data first, which will facilitate and significantly speed up research and clinical efforts by providing instant delivery of data analysis. Augmented reality artificial intelligence software can be added to existing live-cell microscopes, thus providing instant visual feedback with added graphics during sample observation, which will enhance the images by also displaying numbers describing the measured differences and, in doing so, facilitate the image interpretation by the human operator. This will significantly enhance the ability of clinicians to make quick and correct decisions regarding drug action.

There exist very few disease biomarkers allowing for longitudinal *in vivo* analysis like fluorescence puncta in the fundus of the eye. As an extension of the central nervous system, the eye harbors retina ganglion cells vulnerable to degeneration, and visual symptoms are often an early manifestation of neurodegeneration. Imaging the retina, following an intravenous injection of an ocular tracer, allows performing minimally-invasive *in vivo* imaging in patients with a number (over a dozen) of neurodegenerative diseases originating in different areas of the central nervous system. Time-lapse imaging during drug treatment allows for the comparison of the effects of drug regimens on their target proteins. Such companion diagnostics allows to evaluate the relative contribution of different misfolded or aggregated proteins in drug resistance and response; it also allows the discovery of predictive and prognostic biomarkers for the early detection of neurodegeneration and advanced patient stratification analysis. During *in vivo* analysis, retina imaging is associated with rapid three-dimensional rotation but

with on-the-fly registration, a quantitative readout of phenotype changes associated with disease can be delineated in real time. Action recognition algorithms can deliver image segmentation and feature metrics as the basis for predictive and prognostic biomarkers.

Real-time image analysis can also assist surgeons with lesion localization during surgical resections. The software will segment the precise area of selected fiducial biomarkers on-the-fly, enhance the image features of interest, and analyze the time evolution of their contour to improve the precision of the resection boundary. Similarly, it will improve the laser positioning guidance during multi-parametric MRI-guided focal laser ablation therapy. We can envisage many additional applications of our software system, for instance in ultrasound imaging. On-the-fly image contrast enhancement and feature contour display, together with the addition of automated aerial metrics on the screen, will improve the precision of the measurements and diagnosis.

The complexity of current drug regimens in oncology highlights the incredible ability of the neoplastic cell to survive. It suggests the need to develop (easy to use in the clinic) quantitative methods to evaluate drug treatments' short and long-term effects on their cellular target. Often when tumors respond to treatment, the disease eventually returns and, in most cases, does respond to other therapies, even though resistant to the previously given one. This type of drug response indicates that it is crucial to develop tools for optimal drug selection upfront and avoid intrinsic drug resistance as well as anticipate the effects of tumor plasticity and the development of acquired drug resistance. Heterogeneous tumors evolve as a result of drug treatment. During hormonal therapy, cells acquire a loss of the surface expression of their receptor ligands. Very often the drug treatment process would effectively serve as a repeated selection step, allowing for the replication of the most resilient clones. The surviving clone often lacks any known molecular biomarkers for targeted therapy, thus leaving systemic therapy, associated with high toxicity and low cure rates, as, perhaps, the only option. However, drug regimens

approved for other indications can, sometimes serendipitously, induce a full remission and libraries with FDA-approved compounds can routinely be tested in *ex vivo* or *in vivo* quantitative imaging assays to evaluate their drug-target engagement and compare their off-label efficacy. Such an approach can lead to the discovery of putative, secondary mechanisms, which have thus far been not appreciated.

Upon extensive clinical validation, besides anticipating drug resistance, quantitative imaging systems can be utilized to identify sensitizing drugs, targeting the cytoskeleton, to treat disease with known resistant genetic profiles. Further, it will be beneficial to analyze the changes of the cellular phenotype of patient-derived cells of ultimate responders. This way, it will become feasible for quantitative microscopy methods to be used in selecting regimens that achieve complete response and elimination of residual disease.

Given the availability of high-quality fundamental research equipment for high resolution live-cell microscopy in most university hospitals, we propose to embed in these systems real-time augmented reality software for automated quantification and on-the-fly statistical analysis of intracellular behavior. Introducing the quantitative imaging method to the clinic will allow physicians to fine-tune, with a high level of certainty, an optimal treatment regimen for each patient.

The main concern regarding patient treatment, which motivated this work, has been that important differential effects of therapies on their cellular targets pertaining to drug efficacy cannot reliably be identified with genetic sequencing or pathology slides alone. There are differences in the mechanisms with which cells react to treatment, for example in regard to the immune system, which can only be appreciated by live-cell imaging methods. Further, the effects of a physiologically relevant dose of a drug are not visible to the naked eye, looking through the microscope lens, because of the inability of our vision to detect a gradient in pixel intensity when bright features are co-localized with dim features.

In these and many other instances, the cell biology imaging methods require quantification because of the overwhelming number of cellular proteins and components involved. For these reasons, we consider real-time image analysis software as an indispensable tool to extract a truthful readout of the underlying processes.

The potential clinical application of the analytics approach outlined in this manuscript pertains to anticipating drug resistance in cancer therapy and the treatment of neurodegeneration based on the microscopic evaluation of living patient cells *ex vivo*. Until now, the accurate computational analysis of dynamic cytoskeletal structures was limited due to the lack of appropriate software tools. Since the entangled networks in the cell are fast evolving, rapidly changing their turnover rates and directions of motion, it has been a very tedious process for scientists using traditional tracking methods to resolve complex motion patterns. Our method, by not requiring any additional steps for the analysis but rather displaying the tracking vectors in real time, can aid in establishing a new level of insight into cellular processes and, thus, advance our understanding of the dynamic organization of the cytoskeleton, cell division and motility. In doing so, it is our goal to advance the field of drug development and contribute to improving patient care.

MATERIALS AND METHODS

Image analysis

All image analysis programs for detection and tracking of comets, and graphical representation of the results were developed in Matlab and C/C++. The EB1 comet analysis method ClusterTrack used is described and validated in (Matov et al., 2010). The computer code is available for download at: <https://www.github.com/amatov/ClusterTrackTubuline>. The image analysis programs for real-time detection and tracking, and graphical representation of the results were developed in the cross-platform game engine Unity in C#. OpenCV for Unity requires a license from Enox Software. The computer code

is available for download at: <https://www.github.com/amatov/DataSetTracker>. To test the software, we have uploaded EBTracker.exe and DataSetTracker_v1.1.zip files at the same link. In the zip folder, there are instructions on how to test the tracker. It does not require any installations and starts on double click. A default test video is included with the download and the analysis begins upon clicking the software executable file. The user can change the video for analysis.

The Instantaneous Flow Tracking Algorithm, which further describes spot detection algorithms, is described in (Matov, 2024b). The computer code is available for download at: <https://www.github.com/amatov/InstantaneousFlowTracker>.

The 10x image analysis programs for PSMA, α -tubulin, DAPI, and CD45 segmentation as well as 3D AR and DAPI segmentation, and graphical representation of the results were developed in Matlab and C/C++. The wavelet transform method used, spotDetector, was described and validated in (Olivo-Marin, 2002) and the unimodal pixel intensity thresholding in (Rosin, 2001). We identified the CTC areas as connected-component labeling pixel lists in the epithelial tumor imaging channel (such as PSMA or occasionally cytokeratin) for which in the nuclear imaging channel there is a DAPI stain with a statistically representative size and a circular shape. At the same time, we required that these cells are negative in the CD45, i.e., the absence of a leukocyte marker. Similarly, to detect neutrophils and lymphocytes, we identified clusters of bright pixels in the CD45 channel for which a nuclear area is detected in the DAPI channel and the epithelial stain is not present. On multiple occasions, we detected double-positive (PSMA+/DAPI+/CD45+ or CK+/DAPI+/CD45+) and double-negative (PSMA-/DAPI+/CD45- or CK-/DAPI+/CD45-) cells, which we classified in separate bins.

Drug-induced MT bundles were evaluated in terms of thickness and texture parameters in 63x images. The detection of tyrosinated tubulin in 10x images was considered to be a marker of drug sensitivity. We

analyzed the cellular localization of AR in 3D image stacks, in which we performed segmentation in 35 individual 2D images and reconstructed the volume, and classified the CTCs as sensitive to drug treatment if the AR is within the volume of the nucleus and resistant if the AR is mainly in the cytoplasm.

Cell membrane areas in with TGF β -containing secretory granules on the cell surface were identified by image foreground segmentation based on Gaussian filtering (Weierstrass, 1885) with a high value of the standard deviation in order to retain the areas with the fluorescent granules. A unimodal pixel intensity thresholding (Rosin, 2001) was then applied and pixels below the threshold were computationally clipped and set to zero. The resulting images are filtered with a Gaussian kernel with frequency cut-off matched with the limit of the optical transfer function (Fourier, 1822) beyond which the collected signal is white noise and the kernel was computationally fitted to the Bessel function (Bernoulli, 1728) forming the point-spread function of the imaging system. The granules were counted as the number of detected spots as clusters of bright pixels within the area of the segmented cell outline. To this end, we applied a method introduced in (Olivo-Marin, 2002) to detect bright spots in fluorescence images based on the multiscale product of subband images resulting from the à trous wavelet transform (Starck et al., 2000) decomposition of the original image, after thresholding of non-significant coefficients. The multiscale correlation of the altered wavelet coefficients, which allows enhancing multiscale peaks due to spots, while reducing noise, combines information coming from different levels of resolution and gives a clear and distinctive characterization of the spots.

To calculate the overall intensity in immunofluorescence images of MTs in cells growing in clusters, we identify the centroid position of the nucleus by applying unimodal pixel intensity thresholding (Rosin, 2001) in the DAPI channel, which allows the segmentation of the nuclei. We then use the centroids to

build a Voronoi diagram (Dirichlet, 1850) in the MT channel, which provides the watershed lines dividing the individual cells. The computer code is available for download at:

<https://github.com/amatov/SegmentationBiomarkerCTC>,

<https://github.com/amatov/ResistanceBiomarkerAnalysis>,

<https://github.com/amatov/AntibodyTextureMorphology>.

To match baseline AF puncta in fundus images with hyper-fluorescent puncta after injection with fluorescence emitting dye, we utilize speeded-up robust features (SURF) (Bay et al., 2008). In brief, SURF is a scale space-based (Lindeberg, 1993) transform applied at multiple scale for feature detection. For scale selection, the determinant of the Hessian matrix (Hesse, 1872) of second-order partial image derivatives is computed. Features are selected at different scales and Gaussian filtering (Weierstrass, 1885). Feature matching is based on a distance between the descriptor vectors, e.g., the Mahalanobis (Mahalanobis, 1936) or Euclidean distance. The SURF descriptor is computed for a circular region around each feature and consists of intensity distribution of the pixels and feature orientation based on Haar wavelet transform (Haar, 1910) or Gabor filter (Gabor, 1946). The code for analysis of fundus fluorescence is available at: <https://github.com/amatov/NeurodegenerationFluorescentFundus>.

Bioinformatics analysis

Sequence reads were trimmed using Trimmomatic 0.36 (Bolger et al., 2014). We used hg38 genome as reference and aligned the reads with BWA-MEM version 0.7.15 (Li and Durbin, 2010). For variant calling, we utilized SAMtools (Li et al., 2009), BCFtools (Li, 2011), Ensembl Variant Effect Predictor v86 (McLaren et al., 2016), VCFtools (Danecek et al., 2011), and ANNOVAR (Wang et al., 2010). To run the analysis, we installed a virtual machine (Oracle VM Virtual Box 5.0.6) and Ubuntu 12.04.5 on a Windows server with Intel Xeon E5-1620 processor with 4 dual cores and a solid-state drive. For the alignment step, we connected to a high performance computing cluster (Moran, 2016).

Sample processing

Retroperitoneal lymph node organoid whole genome sequencing (736 ng DNA) was done at the UCSF Core Facilities.

Cell culture

All breast cancer cell lines were grown in DMEM (Cellgro, Mediatech) supplemented with 10% FBS (Atlanta Biologicals), incubated at 37°C in 5% CO₂. MT polymerization dynamics was visualized by lentivirus-mediated low level expression of EB1ΔC-2xEGFP (Matov, 2024e), a marker of growing MT plus ends that does not interfere with endogenous EB1 binding partners. The MDA-MB-231 TNBC cells were grown also as 3D cultures in Matrigel (Corning) with MT polymerization dynamics visualized by lentivirus-mediated low level expression of EB1ΔC-2xERFP.

Primary and retroperitoneal lymph node metastatic prostate tumor and sternum metastatic rectal tumor tissues were dissociated to single cells using modified protocols from the Witte lab. Organoids were seeded as single cells in three 30 μL Matrigel drops in 6-well plates. Organoid medium was prepared according to modified protocols from the Clevers lab and the Chen lab.

To obtain a single cell suspension, tissues were mechanically disrupted and digested with 5 mg/ml collagenase in advanced DMEM/F12 tissue culture medium for several hours (between 2 and 12 hours, depending on the biopsy/resection performed). If this step yielded too much contamination with non-epithelial cells, for instance during processing of primary prostate tumors, the protocol incorporated additional washes and red blood cell lysis (Goldstein et al., 2011). Single cells were then counted using a hemocytometer to estimate the number of tumor cells in the sample, and seeded in growth factor-reduced Matrigel drops overlaid with PC medium (Gao et al., 2014). With radical prostatectomy specimens, we had good success with seeding three thousand cells per 30 μl Matrigel drop, but for

metastatic samples organoid seeding could reliably be accomplished with significantly less cells, in the hundreds. To derive organoids from patient CTCs, liquid biopsy samples of 40 ml peripheral blood would be collected, processed, and plated in a Matrigel-Collagen-Fibronectin matrix to form organoids similarly to the metastatic breast cancer organoids we cultured from mouse CTCs (Matov, 2024c).

To transduce organoids, we modified protocols from the Clevers lab to adapt to the specifics of prostate organoid culture (such as the significant differences in proliferation rates in comparison to colon and rectal organoids). We found out empirically that cells in mid-size organoids (60-100 μm in diameter) infect at much better rates than trypsinized single organoid cells. These were the steps we followed to express EB1 Δ C-2xEGFP in organoids: (1) Add Dispase (1 mg/ml) to each well to dissolve the Matrigel at room temperature for 1 hour. (2) Spin down (at 1,000 rpm for 4 minutes) and mix organoids with 10 μl of viral particles (enough for 1 well with three Matrigel drops of 30-40 μl with organoids containing 1-2 million cells) with Y27632 ROCK inhibitor and Polybrene (1:1,000) for 30 minutes. (3) Spin the organoids with viral particles for 1 hour at 600g. (4) Leave the organoids for a 6-hour incubation. (5) Spin down and plate in Matrigel. (6) 1 hour later, add medium. We used blasticidin (1:20,000) for only one round of medium (3 days) because an increase of the density of labeled cells in the organoids reduced our ability to image MT tips with good contrast.

MDA-MB-231 and SK-BR-3 cells were treated with paclitaxel and docetaxel for 2 hours in titration experiments (0.023 nM, 0.69 nM, 0.206 nM, 0.617 nM, 1.852 nM, 5.556 nM, 16.667 nM, 50 nM, and 150 nM) to perform a sulforhodamine B cytotoxicity assay.

MDA-MB-231 cells were pre-treated with 0.1% DMSO (vehicle control) or 100 nM paclitaxel for 6 hours, washed in serum-free DMEM, then treated with 100 $\mu\text{g}/\text{mL}$ lipopolysaccharide in serum-free DMEM for 2 hours to induce TGF β trafficking to the cell membrane. Cells were fixed in PHEMO buffer

(Carbonaro et al., 2011) without any detergent to ensure that cells remained non-permeabilized, then immunostained with a rabbit anti-TGF β antibody, followed by Alexa Fluor 488-conjugated secondary. The total cell area was visualized by counter-staining with a cell membrane dye. TGF β foci were quantified using an adaptation of our blob detection algorithm (Matov, 2024b; Matov et al., 2011). Lipopolysaccharide derived from *Escherichia coli* O111:B4 was obtained from Sigma-Aldrich. Paclitaxel (in intravenous solution) was a gift from Linda Vahdat. Docetaxel was obtained from Sigma-Aldrich in power form.

Microscopy imaging

MDA-MB-231 cells were transfected with plasmid encoding EB1 Δ C-2xEGFP (Piehl and Cassimeris, 2003) and EB1 comets in live cells were imaged by spinning-disc confocal microscopy using a 100x magnification oil immersion 1.49 NA objective for all cultured cells as previously described (Gierke and Wittmann, 2012) and tracked using our image analysis algorithm (Matov et al., 2010). EB1 transiently binds to growing MT plus ends (Akhmanova and Steinmetz, 2008), generating a punctate pattern of EB1 Δ C-2xEGFP comets throughout the cell. The exponential decay of available binding sites results in the characteristic comet-like fluorescence profiles of EGFP-tagged end-binding proteins (“comets”).

Organoids were imaged using transmitted light microscopy at 4x magnification and phase contrast microscopy at 20x magnification on a Nikon Eclipse Ti system with camera Photometrics CoolSnap HQ2.

Ethics declaration

IRB (IRCM-2019-201, IRB DS-NA-001) of the Institute of Regenerative and Cellular Medicine.

Ethical approval was given.

Approval of tissue requests #14-04 and #16-05 to the UCSF Cancer Center Tissue Core and the Genitourinary Oncology Program was given.

Clinical trial number: not applicable.

Data availability statement

The datasets used and/or analyzed during the current study are available from the corresponding author upon reasonable request.

Conflicts of interest

The author declares no conflicts of interest.

Funding statement

No funding was received to assist with the preparation of this manuscript.

ACKNOWLEDGEMENTS

I thank James Cumberbatch (Vidro Ltd) for his help with Unity and XCode, and Neil Bander for the PSMA data. Giuseppe Galletti performed the IC50 experiments. The patient blood samples analyzed were from clinical studies with IRB protocols 0804009740 and 0707009283 at Cornell Medicine. I am grateful to the Genitourinary Tissue Utilization committee and the Genitourinary and Prostate SPORE Tissue Cores at the UCSF Cancer Center for the approval of my tissue requests #14-04 and #16-05, the Stand Up To Cancer / Prostate Cancer Foundation (SU2C/PCF) West Coast Dream Team (WCDT), the Institute of Regenerative and Cellular Medicine for issuing the Institutional Review Board protocol approval IRCM-2019-201, IRB DS-NA-001 for the observational study “Longitudinal analysis of next-generation sequencing of nucleic acids for early detection of degenerative diseases such as

cardiovascular, neoplastic and diseases related to the nervous system”, and James Faber for his feedback regarding the protocol and the process of approval. A preprint of this paper is available at arXiv (Matov, 2024h).

SUPPLEMENTARY MATERIALS

Video 1 – Prostate cancer M12 cell expressing AR-wild type and MT labeling with overlaid EB1 comet detections. <https://vimeo.com/1060977612/ce83b5bd52>

Video 2 – Prostate cancer M12 cell expressing AR-V7 and MT labeling with overlaid EB1 comet detections. <https://vimeo.com/1060978105/1cd7d9779b>

Video 3 – Castrate-resistant prostate cancer organoid cell with MT labeling and EB1 comets. Organoids derived from acetabulum metastasis. <https://vimeo.com/1060978355/812e82c658>

Video 4 – Multiple myeloma exosomes in MM1S cells with labeled CD63.
<https://vimeo.com/1060982925/1c6381fb1f>

Video 5 – Synthetic movie with moving bright features. <https://vimeo.com/999588708/43e6111879>

Video 6 – Overlay of Video 5 with vectors displaying the tracking results.
<https://vimeo.com/999589508/d6dbcf35f5>

Video 7 – Detection of synthetic markers with frame by frame tracks.
<https://vimeo.com/1058382285/00f06c9bb1>

Video 8 – Tracking in epithelial cells with a region of interest selection. The red rectangle shows the selected region of interest. <https://vimeo.com/1058385496/8299567e00>

Video 9 – Tracking in epithelial cells with augmented reality graphics. Histograms showing the distributions of protein speeds and angular orientation are added on the screen during processing. <https://vimeo.com/1058418895/5c6ecf2821>

Video 10 – Tracking in glia cells for glioblastoma drug discovery. Epigenetic histone markers were labeled and track to investigate nuclear reorganization after drug treatment. Shades of red denote the direction of the vectors. Shades of blue denote the different speeds. 19 frames per second are processed. <https://vimeo.com/1058419537/07b1920b97>

Video 11 – Phone app real-time tracking calibration. The video shows testing the phone app during software development. <https://vimeo.com/1058389251/7d6603a5e1>

Video 12 – Tracking via a phone app in real time. Detection is done in real time by pointing the phone toward the computer screen. <https://vimeo.com/1058387386/cdbe5c3d74>

A software folder ‘DataSetTracker_v1.1’ contains the DataSet Tracker executable file, a test video, and a readme file with instructions. You may also download DataSetTracker_v1.1.zip and EBTracker.exe from <https://github.com/amatov/DataSetTracker>. In brief, place EBTracker.exe in the unzipped ‘DataSetTracker_v1.1’ folder and upon double click it will start the real-time analysis of the default MP4 video located in folder ‘Streaming assets’ in ‘EBTracker_Data’.

REFERENCES

- Adams, M., A. Matov, D. Yarar, S. Gupton, G. Danuser, and C.M. Waterman-Storer. 2004. Signal analysis of Total Internal Reflection Fluorescent Speckle Microscopy (TIR-FSM) and widefield epi-fluorescence FSM of the actin cytoskeleton and focal adhesions in living cells. *J. Microsc.* 216:138 - 152.
- Aguilar-Calvo, P., A.M. Sevillano, S. Rasool, K.J. Cao, L.M. Randolph, R.A. Rissman, S.T. Sarraf, J. Yang, and C.J. Sigurdson. 2022. Noninvasive Antemortem Detection of Retinal Prions by a Fluorescent Tracer. *Journal of Alzheimer's disease : JAD.* 88:1137-1145.
- Akhmanova, A., and M.O. Steinmetz. 2008. Tracking the ends: a dynamic protein network controls the fate of microtubule tips. *Nature Reviews Molecular Cell Biology.* 9:309-322.
- Al-Bassam, J., R.S. Ozer, D. Safer, S. Halpain, and R.A. Milligan. 2002. MAP2 and tau bind longitudinally along the outer ridges of microtubule protofilaments. *J Cell Biol.* 157:1187-1196.
- Bay, H., A. Ess, T. Tuytelaars, and L. Van Gool. 2008. Speeded-Up Robust Features (SURF). *Computer vision and image understanding : CVIU.* 110:346-359.
- Bernoulli, D. 1728. Observationes de seriebus recurrentibus. *Novi Commentarii Academiae Scientiarum Imperialis Petropolitanae.* III:85–100.
- Bolger, A.M., M. Lohse, and B. Usadel. 2014. Trimmomatic: a flexible trimmer for Illumina sequence data. *Bioinformatics.* 30:2114-2120.
- Bradski, G. 2000. The OpenCV Library. *Dr Dobb's Journal* 25 (11).
- Bratsun, D., D. Volfson, L.S. Tsimring, and J. Hasty. 2005. Delay-induced stochastic oscillations in gene regulation. 102:14593-14598.
- Bremaud, P. 1999. Gibbs Fields and Monte Carlo Simulation. *Markov Chains.* 31:253–322.
- Brennan, I., A. Matov, G. Danuser, and A. Straight. 2008. Polo-like Kinase Regulation of Anaphase Spindle Elongation. *Molecular biology of the cell.* 19.
- Burkhardt, J.K., J.M. McIlvain, Jr., M.P. Sheetz, and Y. Argon. 1993. Lytic granules from cytotoxic T cells exhibit kinesin-dependent motility on microtubules in vitro. *J Cell Sci.* 104 (Pt 1):151-162.
- Carbonaro, M., A. O'Brate, and P. Giannakakou. 2011. Microtubule disruption targets HIF-1alpha mRNA to cytoplasmic P-bodies for translational repression. *J Cell Biol.* 192:83-99.
- Cattell, R.B. 1943. The measurement of adult intelligence. *Psychological Bulletin.* 40:153–193.
- Danecek, P., A. Auton, G. Abecasis, C.A. Albers, E. Banks, M.A. DePristo, R.E. Handsaker, G. Lunter, G.T. Marth, S.T. Sherry, G. McVean, R. Durbin, and G.P.A. Group. 2011. The variant call format and VCFtools. *Bioinformatics (Oxford, England).* 27:2156-2158.
- de Moivre, A. 1718. The Doctrine of Chances: or, A Method of Calculating the Probability of Events in Play. *W. Pearson.*
- Dirichlet, P.G. 1839. Sur une nouvelle méthode pour la détermination des intégrales multiples. *Journal de Mathématiques Pures et Appliquées.* 4:164-168.
- Dirichlet, P.G. 1850. Über die Reduction der positiven quadratischen Formen mit drei unbestimmten ganzen Zahlen. *Journal für die reine und angewandte Mathematik.* 40:209-227.
- Duda, R.O., and P.E. Hart. 1973. Pattern classification and scene analysis. *Wiley.*
- Ewing, J.A. 1881. On the production of transient electric currents in iron and steel conductors by twisting them when magnetized or by magnetising them when twisted. *Proceedings of the Royal Society of London.* 33:21–23.
- Fisher, R.A. 1912. On an absolute criterion for fitting frequency curves. *Messenger of Mathematics.* 41:155-160.
- Fourier, J.B.J. 1822. Théorie Analytique de la Chaleur. *Chez Firmin Didot, Pere et Fils.*
- Gabor, D. 1946. Theory of communication. *Journal of the Institution of Electrical Engineers.* 93.
- Galletti, G., A. Matov, H. Beltran, J. Fontugne, J. Miguel Mosquera, C. Cheung, T.Y. MacDonald, M. Sung, S. O'Toole, J.G. Kench, S. Suk Chae, D. Kimovski, S.T. Tagawa, D.M. Nanus, M.A.

- Rubin, L.G. Horvath, P. Giannakakou, and D.S. Rickman. 2014. ERG induces taxane resistance in castration-resistant prostate cancer. *Nature communications*. 5:5548.
- Gao, D., I. Vela, A. Sboner, P.J. Iaquina, W.R. Karthaus, A. Gopalan, C. Dowling, J.N. Wanjala, E.A. Undvall, V.K. Arora, J. Wongvipat, M. Kossai, S. Ramazanoglu, L.P. Barboza, W. Di, Z. Cao, Q.F. Zhang, I. Sirota, L. Ran, T.Y. MacDonald, H. Beltran, J.M. Mosquera, K.A. Touijer, P.T. Scardino, V.P. Laudone, K.R. Curtis, D.E. Rathkopf, M.J. Morris, D.C. Danila, S.F. Slovin, S.B. Solomon, J.A. Eastham, P. Chi, B. Carver, M.A. Rubin, H.I. Scher, H. Clevers, C.L. Sawyers, and Y. Chen. 2014. Organoid cultures derived from patients with advanced prostate cancer. *Cell*. 159:176-187.
- Gatlin, J.C., A. Matov, G. Danuser, T.J. Mitchison, and E.D. Salmon. 2010. Directly probing the mechanical properties of the spindle and its matrix. *Journal of Cell Biology*. 188:481-489.
- Gatlin, J.C., A. Matov, A.C. Groen, D.J. Needleman, T.J. Maresca, G. Danuser, T.J. Mitchison, and E.D. Salmon. 2009. Spindle Fusion Requires Dynein-Mediated Sliding of Oppositely Oriented Microtubules. *Current Biology*. 19:287-296.
- Gauss, C.F. 1809. *Theoria motus corporum coelestium in sectionibus conicis solem ambientum. Hamburgi, Sumtibus F. Perthes et I.H. Besser.*
- Gierke, S., and T. Wittmann. 2012. EB1-recruited microtubule +TIP complexes coordinate protrusion dynamics during 3D epithelial remodeling. *Current biology : CB*. 22:753-762.
- Gillespie, D.T. 2007. Stochastic Simulation of Chemical Kinetics. 58:35-55.
- Goldstein, A.S., J.M. Drake, D.L. Burnes, D.S. Finley, H. Zhang, R.E. Reiter, J. Huang, and O.N. Witte. 2011. Purification and direct transformation of epithelial progenitor cells from primary human prostate. *Nature protocols*. 6:656-667.
- Gompertz, B. 1825. On the Nature of the Function Expressive of the Law of Human Mortality, and on a New Mode of Determining the Value of Life Contingencies. *Philosophical Transactions of the Royal Society of London*. 115:513-583.
- Haar, A. 1910. Zur Theorie der orthogonalen Funktionensysteme. *Mathematische Annalen*. 69:331-371.
- Hangauer, M.J., V.S. Viswanathan, M.J. Ryan, D. Bole, J.K. Eaton, A. Matov, J. Galeas, H.D. Dhruv, M.E. Berens, S.L. Schreiber, F. McCormick, and M.T. McManus. 2017. Drug-tolerant persister cancer cells are vulnerable to GPX4 inhibition. *Nature*. 551:247-250.
- Harkcom, W.T., A.K. Ghosh, M.S. Sung, A. Matov, K.D. Brown, P. Giannakakou, and S.R. Jaffrey. 2014. NAD⁺ and SIRT3 control microtubule dynamics and reduce susceptibility to antimicrotubule agents. *Proceedings of the National Academy of Sciences of the United States of America*. 111:E2443-2452.
- Hesse, L.O. 1872. *Die Determinanten elementar behandelt. Teubner.*
- Houghtaling, B.R., G. Yang, A. Matov, G. Danuser, and T.M. Kapoor. 2009. Op18 Reveals the Contribution of Non-Kinetochore Microtubules to the Dynamic Organization of the Vertebrate Meiotic Spindle. *Proc Natl Acad Sci U S A*. 106:15338-15343.
- Hwang, S.J., H.W. Lee, H.R. Kim, H.J. Song, D.H. Lee, H. Lee, C.H. Shin, J.G. Joung, D.H. Kim, K.M. Joo, and H.H. Kim. 2015. Overexpression of microRNA-95-3p suppresses brain metastasis of lung adenocarcinoma through downregulation of cyclin D1. *Oncotarget*. 6:20434-20448.
- Jungius, J. 1622. *Heuretica. Societas Ereunetica.*
- Kakade, S., and J. Langford. 2002. Approximately Optimal Approximate Reinforcement Learning. In *Proceedings of the Nineteenth International Conference on Machine Learning*. Morgan Kaufmann Publishers Inc. 267-274.
- Kumar, P., K.S. Lyle, S. Gierke, A. Matov, G. Danuser, and T. Wittmann. 2009. GSK3 β phosphorylation modulates CLASP-microtubule association and lamella microtubule attachment. *The Journal of Cell Biology*. 184:895-908.
- Lagrange, J.-L. 1788. *Mécanique analytique. Ve Courcier.*

- Lasserre, R., and A. Alcover. 2012. Microtubule dynamics and signal transduction at the immunological synapse: new partners and new connections. *The EMBO journal*. 31:4100-4102.
- Legendre, A.-M. 1805. Nouvelles méthodes pour la détermination des orbites des comètes. *F. Didot*.
- Li, H. 2011. A statistical framework for SNP calling, mutation discovery, association mapping and population genetical parameter estimation from sequencing data. *Bioinformatics (Oxford, England)*. 27:2987-2993.
- Li, H., and R. Durbin. 2010. Fast and accurate long-read alignment with Burrows-Wheeler transform. *Bioinformatics (Oxford, England)*. 26:589-595.
- Li, H., B. Handsaker, A. Wysoker, T. Fennell, J. Ruan, N. Homer, G. Marth, G. Abecasis, and R. Durbin. 2009. The Sequence Alignment/Map format and SAMtools. *Bioinformatics (Oxford, England)*. 25:2078-2079.
- Lindeberg, T. 1993. Detecting Salient Blob-Like Image Structures and Their Scales with a Scale-Space Primal Sketch: A Method for Focus-of-Attention. *International Journal of Computer Vision* 11:283–318.
- Lucas, B.D., and T. Kanade. 1981. An iterative image registration technique with an application in stereo vision. *International Conference on Artificial Intelligence*:674 - 679.
- Mahalanobis, P.C. 1936. On the Generalised Distance in Statistics. *Journal of The Asiatic Society of Bengal*. 80:1-7.
- Matov, A. 1999. Capacity Region Characterization of Multi-User Parallel Gaussian Broadcast Channels. *Swiss Federal Institute of Technology Lausanne*:1-41.
- Matov, A. 2024a. Analysis of Multiple Myeloma Drug Efficacy. *medRxiv*:2024.24311450.
- Matov, A. 2024b. Analysis of Unstructured High-Density Crowded Scenes for Crowd Monitoring. *arXiv*:2408.11836.
- Matov, A. 2024c. Computational Analysis of Treatment Resistant Cancer Cells. *medRxiv*:2024.24312813.
- Matov, A. 2024d. Microtubule Regulation in Cancer Cells *SSRN*:2024.5072927.
- Matov, A. 2024e. Mitosis, Cytoskeleton Regulation, and Drug Resistance in Receptor Triple Negative Breast Cancer. *arXiv*:2407.19112.
- Matov, A. 2024f. Modulation of the Cytoskeleton for Cancer Therapy *SSRN*:2024.5061950.
- Matov, A. 2024g. Quantitative Video Microscopy in Medicine. *SSRN*:2024.4909311.
- Matov, A. 2024h. Real-Time Image Analysis Software Suitable for Resource-Constrained Computing. *arXiv*:2407.15735.
- Matov, A. 2024i. Urinary Biomarkers for Lung Cancer Detection. *medRxiv*:2024.24311186.
- Matov, A. 2025a. Microtubule Dysregulation in Prostate Cancer Metastasis to the Vertebrae *SSRN*:2025.5112427.
- Matov, A. 2025b. Quantitative Cell Division and Migration in Medicine. *SSRN*:2025.5130515.
- Matov, A., K. Applegate, P. Kumar, C.R. Thoma, W. Krek, G. Danuser, and T. Wittmann. 2010. Analysis of microtubule dynamic instability using a plus end growth marker. *Nature Methods*. 7:761-768.
- Matov, A., and A. Bacconi. 2024. Measurements of Contractility in Actin Convergence Zone and KIF11-Inhibited Mitotic Spindles. *bioRxiv*:2024.601275.
- Matov, A., and G. Danuser. 2004. Tracking faint features in fluorescent speckle microscopy to probe microtubule flux in mitotic spindles. *Scripps Research*.
- Matov, A., J. de Rooij, J.C. Gatlin, J. Rohrberg, N. Ahmad, R. Aggarwal, J. Simko, A. Goga, C.J. Ryan, and T. Wittmann. 2016. Investigating microtubule growth dynamics in patient-derived metastatic prostate cancer cells. *Cancer Research*. 76:243.
- Matov, A., M.M. Edvall, G. Yang, and G. Danuser. 2011. Optimal-Flow Minimum-Cost Correspondence Assignment in Particle Flow Tracking. *Computer vision and image understanding : CVIU*. 115:531-540.

- Matov, A., J. Rohrberg, A. Goga, and T. Wittmann. 2015. Investigating Microtubule Growth Dynamics and Spindle Positioning Regulation in Breast Cancer Cells. *Molecular biology of the cell*. 26.
- McLaren, W., L. Gil, S.E. Hunt, H.S. Riat, G.R. Ritchie, A. Thormann, P. Flicek, and F. Cunningham. 2016. The Ensembl Variant Effect Predictor. *Genome biology*. 17:122.
- Men, L., D. Nie, and H. Nie. 2019. microRNA-577 inhibits cell proliferation and invasion in non-small cell lung cancer by directly targeting homeobox A1. *Molecular medicine reports*. 19:1875-1882.
- Moran, M. 2016. Advanced Research Computing Center, Laramie, WY. doi.org/10.15786/M2FY47. University of Wyoming.
- Ni, J., X. Zhang, J. Li, Z. Zheng, J. Zhang, W. Zhao, and L. Liu. 2021. Tumour-derived exosomal lncRNA-SOX2OT promotes bone metastasis of non-small cell lung cancer by targeting the miRNA-194-5p/RAC1 signalling axis in osteoclasts. *Cell death & disease*. 12:662.
- Olivo-Marin, J.-C. 2002. Extraction of spots in biological images using multiscale products. *Pattern Recogn.* 35:1989-1996.
- Ong, J., A. van den Berg, A. Faiz, I.M. Boudewijn, W. Timens, C.J. Vermeulen, B.G. Oliver, K. Kok, M.M. Terpstra, M. van den Berge, C.A. Brandsma, and J. Kluiver. 2019. Current Smoking is Associated with Decreased Expression of miR-335-5p in Parenchymal Lung Fibroblasts. *International journal of molecular sciences*. 20.
- Piehl, M., and L. Cassimeris. 2003. Organization and dynamics of growing microtubule plus ends during early mitosis. *Molecular biology of the cell*. 14:916-925.
- Pilotte, J., A.S. Huang, S. Houry, X. Zhang, A. Tafreshi, P. Vanderklish, S.T. Sarraf, J.S. Pulido, and T. Milman. 2024. Detection of TTR Amyloid in the Conjunctiva Using a Novel Fluorescent Ocular Tracer. *Translational vision science & technology*. 13:11.
- Pilotte, J., S. Houry, A. Tafreshi, Z.T. Mandel, S.V. Sharma, P.W. Vanderklish, S.T. Sarraf, A.A. Sadun, R.N. Weinreb, and A.S. Huang. 2025. Identification of Retinal Amyloid-Beta in Ex Vivo Human Glaucoma Eyes Using a Novel Ocular Tracer. *Journal of glaucoma*. 34:e4-e8.
- Ponti, A., A. Matov, M. Adams, S. Gupton, C.M. Waterman-Storer, and G. Danuser. 2005. Periodic patterns of actin turnover in lamellipodia and lamellae of migrating epithelial cells analyzed by Quantitative Fluorescent Speckle Microscopy. *Biophys. J.* 89:3456-3469.
- Ponti, P., P. Vallotton, A. Matov, C.M. Waterman-Storer, E.D. Salmon, and G. Danuser. 2003. Computational Fluorescence Speckle Microscopy. *Biophysical Journal*. 84:439A-439A.
- Potenta, S., E. Zeisberg, and R. Kalluri. 2008. The role of endothelial-to-mesenchymal transition in cancer progression. *British journal of cancer*. 99:1375-1379.
- Pulli, K., A. Baksheev, K. Korniyakov, and V. Eruhimov. 2012. Real-Time Computer Vision with OpenCV *Communications of the ACM*. 55:61 - 69.
- Rosin, P.L. 2001. Unimodal thresholding. *Pattern Recognition*. 34:2083 - 2096.
- Schneider, S., and D.H. Wagner. 1957. Error detection in redundant systems. In Papers presented at the February 26-28, 1957, western joint computer conference: Techniques for reliability. Association for Computing Machinery, Los Angeles, California. 115-121.
- Schulman, J., S. Levine, P. Moritz, M. Jordan, and P. Abbeel. 2015. Trust region policy optimization. In Proceedings of the 32nd International Conference on International Conference on Machine Learning - Volume 37. JMLR.org, Lille, France. 1889-1897.
- Schulman, J., F. Wolski, P. Dhariwal, A. Radford, and O. Klimov. 2017. Proximal Policy Optimization Algorithms. *ArXiv:1707.06347*.
- Shao, Z., P. Wang, Q. Zhu, R. Xu, J. Song, X. Bi, H. Zhang, M. Zhang, Y.K. Li, Y. Wu, and D. Guo. 2024. DeepSeekMath: Pushing the Limits of Mathematical Reasoning in Open Language Models. *arXiv:2402.03300*.
- Shi, J., and C. Tomasi. 1994. Good features to track. *IEEE Conference on Computer Vision and Pattern Recognition:593 - 600*.

- Shitara, K., Y.J. Bang, S. Iwasa, N. Sugimoto, M.H. Ryu, D. Sakai, H.C. Chung, H. Kawakami, H. Yabusaki, J. Lee, K. Saito, Y. Kawaguchi, T. Kamio, A. Kojima, M. Sugihara, and K. Yamaguchi. 2020. Trastuzumab Deruxtecan in Previously Treated HER2-Positive Gastric Cancer. *N Engl J Med.* 382:2419-2430.
- Skipper, H.E., F.M. Schabel, Jr., and W.S. Wilcox. 1964. Experimental Evaluation of Potential Anticancer Agents. XIII. On the Criteria and Kinetics Associated with "Curability" of Experimental Leukemia. *Cancer chemotherapy reports.* 35:1-111.
- Spanjaard, E., I. Smal, N. Angelopoulos, I. Verlaan, A. Matov, E. Meijering, L. Wessels, H. Bos, and J. de Rooij. 2015. Quantitative imaging of focal adhesion dynamics and their regulation by HGF and Rap1 signaling. *Experimental cell research.* 330:382-397.
- Starck, J.-L., F. Murtagh, and A. Bijaoui. 2000. Image Processing and Data Analysis: The Multiscale Approach. *Cambridge Press.*
- Tan, I.B., T. Ivanova, K.H. Lim, C.W. Ong, N. Deng, J. Lee, S.H. Tan, J. Wu, M.H. Lee, C.H. Ooi, S.Y. Rha, W.K. Wong, A. Boussioutas, K.G. Yeoh, J. So, W.P. Yong, A. Tsuburaya, H. Grabsch, H.C. Toh, S. Rozen, J.H. Cheong, S.H. Noh, W.K. Wan, J.A. Ajani, J.S. Lee, M. Salto-Tellez, and P. Tan. 2011. Intrinsic Subtypes of Gastric Cancer, Based on Gene Expression Pattern, Predict Survival and Respond Differently to Chemotherapy. *Gastroenterology.* 141:476-485.e411.
- Thoma, C.R., A. Matov, K.L. Gutbrodt, K.R. Hoerner, W. Krek, and G. Danuser. 2010. Quantitative image analysis identifies pVHL as a key regulator of microtubule dynamic instability. *Journal of Cell Biology.* 190:991-1003.
- Tran, A., K. Kita, A. Matov, D.C. Hassane, L.M. Brown, and P. Giannakakou. 2013. Microtubule stabilization alters tumor secretome and fibroblast activation. *Cancer Research.* 73:5162-5162.
- Tran, A., A. Matov, M. Sung, L. Brown, D.C. Hassane, and P. Giannakakou. 2012. Microtubules regulate tumor microenvironment remodeling. *Understanding Cancer: Genomes to Devices Symposium, New York Academy of Medicine.*
- Unity. 2017. Unity Technologies. *Game development platform.* //unity.com/.
- Vaswani, A., N. Shazeer, N. Parmar, J. Uszkoreit, L. Jones, A.N. Gomez, Ł. Kaiser, and I. Polosukhin. 2017. Attention is all you need. In *Proceedings of the 31st International Conference on Neural Information Processing Systems.* Curran Associates Inc., Long Beach, California, USA. 6000–6010.
- Vichai, V., and K. Kirtikara. 2006. Sulforhodamine B colorimetric assay for cytotoxicity screening. *Nat Protoc.* 1:1112-1116.
- Viswanathan, V.S., M.J. Ryan, H.D. Dhruv, S. Gill, O.M. Eichhoff, B. Seashore-Ludlow, S.D. Kaffenberger, J.K. Eaton, K. Shimada, A.J. Aguirre, S.R. Viswanathan, S. Chattopadhyay, P. Tamayo, W.S. Yang, M.G. Rees, S. Chen, Z.V. Boskovic, S. Javaid, C. Huang, X. Wu, Y.Y. Tseng, E.M. Roider, D. Gao, J.M. Cleary, B.M. Wolpin, J.P. Mesirov, D.A. Haber, J.A. Engelman, J.S. Boehm, J.D. Kotz, C.S. Hon, Y. Chen, W.C. Hahn, M.P. Levesque, J.G. Doench, M.E. Berens, A.F. Shamji, P.A. Clemons, B.R. Stockwell, and S.L. Schreiber. 2017. Dependency of a therapy-resistant state of cancer cells on a lipid peroxidase pathway. *Nature.* 547:453-457.
- Wallace, C.S., and D.M. Boulton. 1968. An Information Measure for Classification. *The Computer Journal.* 11:85–194.
- Wallis, J. 1685. A Treatise of Algebra, both Historical and Practical. *University of Oxford.*
- Wang, K., M. Li, and H. Hakonarson. 2010. ANNOVAR: functional annotation of genetic variants from high-throughput sequencing data. *Nucleic acids research.* 38:e164.
- Weierstrass, K. 1885. Über die analytische Darstellbarkeit sogenannter willkürlicher Functionen einer reellen Veränderlichen. *Sitzungsberichte der Königlich Preußischen Akademie der Wissenschaften.* II.

- Winsor, C.P. 1932. The Gompertz Curve as a Growth Curve. *Proceedings of the National Academy of Sciences of the United States of America*. 18:1-8.
- Xie, W., Y. Wang, Y. Huang, H. Yang, J. Wang, and Z. Hu. 2009. Toll-like receptor 2 mediates invasion via activating NF-kappaB in MDA-MB-231 breast cancer cells. *Biochemical and biophysical research communications*. 379:1027-1032.
- Yang, G., A. Matov, and G. Danuser. 2005. Reliable tracking of large scale dense antiparallel particle motion for fluorescence live cell imaging. *In Proc. IEEE Computer Vision and Pattern Recognition*, San Diego. 138-146.
- Zhan, Y., L. Li, C. Guo, Y. Zhang, L. Zhao, Z. Tao, H. Zhang, and S. Chen. 2024. MicroRNA-141-3p reduces pulmonary hypoxia/reoxygenation injury through suppression of Beclin-1-dependent autophagy. *Aging*. 16:1352-1373.
- Zhang, K., X. Han, W. Hu, C. Su, and B. He. 2022. miR-29a-3p inhibits the malignant characteristics of non-small cell lung cancer cells by reducing the activity of the Wnt/ β -catenin signaling pathway. *Oncology letters*. 24:379.
- Zhang, Q., K. Zheng, Y. Gao, S. Zhao, Y. Zhao, W. Li, Y. Nan, Z. Li, W. Liu, X. Wang, Y. Chen, G. Liu, and F. Jin. 2023. Plasma exosomal miR-1290 and miR-29c-3p as diagnostic biomarkers for lung cancer. *Heliyon*. 9:e21059.
- Zivkovic, Z. 2004. Improved adaptive Gaussian mixture model for background subtraction. *International Conference on Pattern Recognition*. 2:28 - 31.
- Zivkovic, Z. 2006. Efficient adaptive density estimation per image pixel for the task of background subtraction. *Pattern Recognition Letters*. 27:773 - 780.